Effect of Design on Human Injury and Fatality Due to Impacts by Small UAS

Rattanagraikanakorn, Borrdephong ; Blom, H.A.P.; Gransden, Derek I.; Schuurman, M.J.; de Wagter, C.; Sharpanskykh, Alexei; Happee, R.

Article

Effect of Design on Human Injury and Fatality Due to Impacts by Small UAS

Borrdephong Rattanagraikanakorn [1,*], Henk A. P. Blom [2], Derek I. Gransden [3], Michiel Schuurman [4], Christophe De Wagter [5], Alexei Sharpanskykh [6] and Riender Happee [7]

[1] Faculty of Engineering, Chulalongkorn University, Phayathai Road, Pathumwan, Bangkok 10330, Thailand
[2] Section Air Transport and Operation, Faculty of Aerospace Engineering, Delft University of Technology, Kluyverweg 1, 2629 HS Delft, The Netherlands; h.a.p.blom@tudelft.nl
[3] Mechanical and Aerospace Engineering, Carleton University, Canal Building Room 4311, Ottawa, ON K1S 5B6, Canada; derekgransden@cunet.carleton.ca
[4] Aerospace Structures & Materials Department, Faculty of Aerospace Engineering, Delft University of Technology, Kluyverweg 1, 2629 HS Delft, The Netherlands; michiel@schuurman-aero.com
[5] MavLab, Faculty of Aerospace Engineering, Delft University of Technology, Kluyverweg 1, 2629 HS Delft, The Netherlands; c.dewagter@tudelft.nl
[6] Faculty of Aerospace Engineering Section Air Transport and Operation, Delft University of Technology, Kluyverweg 1, 2629 HS Delft, The Netherlands; o.a.sharpanskykh@tudelft.nl
[7] Cognitive Robotics, Faculty of Mechanical Engineering, Delft University of Technology, Mekelweg 2, 2628 CD Delft, The Netherlands; r.happee@tudelft.nl
* Correspondence: borrdephong.p@chula.ac.th; Tel.: +66-83-515-1982

Abstract

Although Unmanned Aircraft Systems (UASs) offer valuable services, they also introduce certain risks—particularly to individuals on the ground—referred to as third-party risk (TPR). In general, ground-level TPR tends to rise alongside the density of people who might use these services, leading current regulations to heavily restrict UAS operations in populated regions. These operational constraints hinder the ability to gather safety insights through the conventional method of learning from real-world incidents. To address this, a promising alternative is to use dynamic simulations that model UAS collisions with humans, providing critical data to inform safer UAS design. In the automotive industry, the modelling and simulation of car crashes has been well developed. For small UAS, this dynamical modelling and simulation approach has focused on the effect of the varying weight and kinetic energy of the UAS, as well as the geometry and location of the impact on a human body. The objective of this research is to quantify the effects of UAS material and shape on-ground TPR through dynamical modelling and simulation. To accomplish this objective, five camera–drone types are selected that have similar weights, although they differ in terms of airframe structure and materials. For each of these camera–drones, a dynamical model is developed to simulate impact, with a biomechanical human body model validated for impact. The injury levels and probability of fatality (PoF) results, obtained through conducting simulations with these integrated dynamical models, are significantly different for the camera–drone types. For the uncontrolled vertical impact of a 1.2 kg UAS at 18 m/s on a model of a human head, differences in UAS designs even yield an order in magnitude difference in PoF values. Moreover, the highest PoF value is a factor of 2 lower than the parametric PoF models used in standing regulation. In the same scenario for UAS types with a weight of 0.4 kg, differences in UAS designs even considered yield an order when regarding the magnitude difference in PoF values. These findings confirm that the material and shape design of a UAS plays an important role in reducing ground TPR, and that these effects can be addressed by using dynamical modelling and simulation during UAS design.

1. Introduction

Unmanned Aircraft Systems (UASs) have experienced rapid growth across both civilian and industrial sectors, supporting applications such as infrastructure inspection, precision agriculture, parcel delivery, emergency response, and aerial surveillance [1–6]. As these systems become more autonomous and capable—driven by advances in navigation algorithms, artificial intelligence, and fault-tolerant control strategies [7–9]—their integration into densely populated environments is accelerating. With increasing drone deployment, this will be increasingly relevant as the imposed level of ground third-party risk (TPR) typically increases linearly with the density of potential customers of UAS services. Standing regulation [10,11] poses significant limitations on the operation of commercial UAS services in populated areas, as a result of which human society is hardly exposed to ground TPR by UASs. The restricted operational exposure, combined with the absence of structured reporting for UAS-related accidents, hampers the conventional method of improving safety through incident analysis. As a more proactive alternative, model-based safety risk assessment offers a valuable approach for generating safety insights that can inform both UAS design and operational practices. As is well explained in [12], current regulation is based on conservative parametric models, e.g., [13,14], that focus on kinetic energy of an impacting UAS. The good news is that regulators, e.g., JARUS [10], offer an open door for the use of improved ground TPR assessment methodology.

In the automotive industry, the common vehicle design practice is to conduct car crash tests in a laboratory with the use of a well-developed human dummy, referred to as a Hybrid III male dummy, and to complement these laboratory tests with computer simulations of the interaction of a human body with car structures during a crash. For the simulation approach, two well-developed and validated simulation packages are widely used: THUMS (Total Human Model for Safety) [15] and MADYMO (Mathematical Dynamic Model) [16]. THUMS makes use of Finite Element (FE) models of the crashing car and the human involved, whereas MADYMO makes use of multibody system (mBS) models. A logical research question is whether these crash testing and dynamical simulation approaches can also be effectively used in UAS ground TPR assessment.

This research question has been addressed by ASSURE (Alliance for System Safety of UAS through Research Excellence). Arterburn et al. [17] report and compare three types of ASSURE results: (i) crash tests with various UAS types on a Hybrid III male dummy; (ii) FE modelling and simulation of various UAS types within THUMS [15]; (iii) measurements of head kinematics during controlled UAS hitting a Postmortem Human Surrogate (PMHS). For all three types of results, they show that in addition to kinetic energy, there is significant dependence on impact geometry (UAS orientation, body location, and impact angle). A comparison of the results for two small UAS types (DJI Phantom III and eBee+) shows the similarity of the outcomes of (i) crash tests and (ii) FE simulations, though notable discrepancies are observed when compared with (iii) the head kinematics data from PMHS impact tests [17]. Complementing these findings, Svatý et al. [18] conducted 49 vertical drop tests using UASs of varying masses (20 g–1 kg) on a Hybrid III dummy and demonstrated that injury risk cannot be reliably assessed by kinetic energy alone; rather, metrics like HIC, structural compliance, and energy dissipation during impact offer more predictive insights into head trauma outcomes.

Independent of this ASSURE research, Rattanagraikanakorn et al. [19] developed an MBS model of DJI Phantom III, and conducted MBS simulations with MADYMO of hitting a male human body as well as a Hybrid III dummy under various impact geometries. Comparison of the simulated head kinematics of the human body versus Hybrid III dummy showed large differences similar to those identified by [17]. The similarity of these findings stems, in both cases, from the fact that the head–neck behaviour of the Hybrid III dummy differs significantly from that of a human body, unless the hitting is frontal and in a horizontal direction. Recently, Weng et al. [20] conducted dynamical simulations with an FE model of DJI Phantom III hitting aversion 4.02 of a male human body model [21]. The obtained simulation results for head kinematics have been shown to correspond much better with the PMHS hitting results shown in [22,23].

Motivated by the above findings, refs. [24–26] used this dynamical modelling and simulation approach for a parcel delivery UAS hitting a human. Wang et al. [25] developed an FE model for a UAS measuring 4.5 kg and integrated this with THUMS to assess human injury levels. Li et al. [26] assessed human injury levels for a parcel delivery UAS measuring 20.5 kg by conducting FE model simulations with THUMS. In comparison to DJI Phantom III, measuring 1.2 kg, the head and neck kinematics increase by an order of magnitude, as a result of which this parcel delivery drone may only fly over less populated areas. To study the mitigation of the latter restriction, Jiang et al. [24] used MADYMO to study the effect of a deployable parachute and airbag for a parcel delivery UAS measuring 15 kg.

The overall conclusion drawn from the above-described research is that during the design of a UAS, effective use of TPR assessment obtained through the dynamical simulation of MBS models within MADYMO [16] or of FE models within THUMS [21] can be achieved. This opens the door to the use of these dynamical simulation platforms to study the effect of other design issues, such as the material and shape of a UAS. Since this design aspect has not yet received proper attention, the objective of the current research is to evaluate, through dynamical modelling and simulation, what the effect of varying the material and shape of a UAS is.

To accomplish this objective, in addition to DJI Phantom III, four additional camera–drone types were selected that differ in frame materials such as carbon fibre, ABS plastic, and polystyrene foam. Table 1 gives an overview of the characteristics of the resulting five camera–drones. The selected DJI F450 and Tarot LJI 500 camera–drones have a similar weight to DJI Phantom III, though they differ significantly in their materials. The selected Parrot Bebop and True XS Racing add different material properties and operating speeds for camera drones having a factor 3 lower weight than DJI Phantom III.

This paper is organized as follows. Section 2 describes the MBS modelling and calibration steps that are conducted for each of the four novel UAS types, as well as their integration with the human body model of MADYMO and the injury criteria used. Section 3 develops two prominent UAS collision scenarios to be simulated with the MBS models, i.e., UAS-controlled horizontal collision with a human head and UAS-uncontrolled vertical drop on a human head. Sections 4 and 5 present the simulation results and discussion for these two encounter scenarios, respectively. Section 6 presents the conclusion of this paper.

In Appendix A, a comparison is made between the test results on the DJI Phantom III impacts on PMHS [22] and the MBS model simulation results for impacts under equal geometric conditions. Based on the analysis in Appendix A it is concluded that the two results are quite similar, with a relatively small (11%) underestimation, on average, by the MBS model, of the head injury metric only. This small but systematic difference of an 11% underestimation is compensated for in Sections 4 and 5 of this paper for all five UAS types.

Table 1. Summary of weight, maximum speed, and design characteristics of selected UAS types.
* Price range reflects variations in components and configurations among DIY/custom builds.

UAS Type	Total Weight [kg]	Max. Speed [m/s]	Configuration	Airframe Materials	Airframe Design	Estimated Cost
DJI Phantom III (Baseline)	1.21	18		ABS Plastic	Sandwich shell structure	~USD 00
DJI F450	1.16	18	Quadcopter with camera gimbal system	ABS Plastic	Sandwich plate structure with moulded plastic motor arm	~USD 500 (kit estimate) *
Tarot LJI500	1.18	18		Carbon Fibre	Sandwich plate structure with carbon fibre rod as motor arm	~USD 450 (kit estimate) *
Parrot Bebop	0.40	16	Quadcopter with front camera cover with polystyrene foam	ABS Plastic	Moulded ABS plastic structure	~USD 500
TrueXS Racing UAS	0.40	48	Racing quadcopter with onboard camera	Carbon Fibre	Sandwich plate structure of thick laminates, including motor arm	USD 200–500 (custom build) *

2. MBS Model Development to Simulate UAS Interactions with Human Body

2.1. MBS Model Development Activities

For each of the four newly selected UASs, MBS models will be constructed and integrated within MADYMO. The activities through which to accomplish this are similar to those conducted for DJI Phantom III by Rattanagraikanakorn et al. [27].

The first activity is to decompose a specific UAS into multiple rigid bodies representing key structural elements, such as the main frame, motor arms, and the camera gimbal. The identified structural elements are mapped into an MBS network of rigid bodies, kinematic joints, and force restraints. For each structural element, the mass and geometric dimensions are obtained through straightforward measurements of the physical UAS parts. Section 2.2 describes the results obtained during this first step for each of the five UAS types.

The second activity is to conduct quasi-static compression tests to evaluate force–displacement characteristics, which provide essential stiffness and damping values for the joints. Also, a ground vibration test (GVT) is performed to estimate natural frequencies and derive damping coefficients. The results of these second activities are described in Section 2.3.
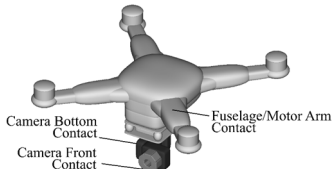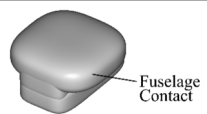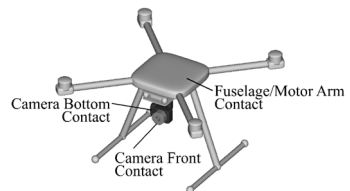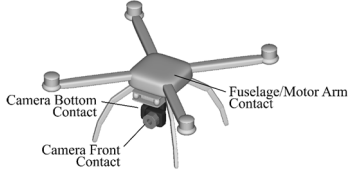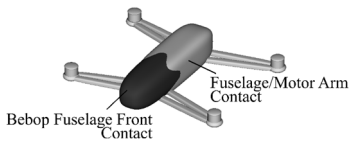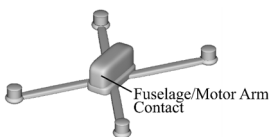
The third activity is to assign ellipsoidal contact surfaces to each identified UAS body; this allows us to represent an external geometry and enable contact force modelling. The latter also includes models of spring–damper restraints to account for structural deformations and energy dissipation during impact. For each contact surface between the MBS model and human head, a force–penetration contact model is used to account for both external and internal contacts. The external contact model is defined in terms of Hertzian elastic contact mechanics. For the internal contact model, which accounts for interactions between drone components such as the damp plate and gimbal assembly, an elastic–perfectly plastic contact model is used, incorporating the specifics of the contact stiffness values of the applicable UAS material, such as carbon fibre, plastic, or foam. The results of this third step are described in Section 2.4.

The fourth activity is to adopt the MADYMO's MBS model of a 50-percentile male human body, and to also describe the injury metric adopted for human head kinematics during a simulated interaction of an impacting UAS. This fourth step is described in Section 2.5. The final step is to characterize the mapping of head injury metrics from the fourth step to probability of fatality; this is accomplished in Section 2.6.

2.2. UAS Multibody System Models

For each UAS type, and also for a Hypothetical UAS with a stiff structure, an MBS model is developed. Table 2 shows images of these six UAS types and their MBS views. For DJI Phantom III, the MBS model of [27] is used; it is explained that DJI Phantom III landing gears are so flexible that their impact is negligible, and therefore they are not included in the DJI Phantom III MBS model.

Table 2. Real-world views and MBS views of the five + one UAS types considered. Note that the landing gears in the real-world view of DJI Phantom III are not in its MBS view; there is no real-world view for the Hypothetical UAS. The real-world views of Tarot LJI500 and DJI F450 are without a camera gimbal, while their MBS views include the camera gimbal of DJI Phantom III.

Weight Class	UAS Type	Real-World View	Multibody System View
	DJI Phantom III (Baseline)		
	Hypothetical UAS	N/A	
Mid-size UAS ($W_0 \approx 1.2$ kg)	Tarot LJI500		
	DJI F450		
Micro UAS ($W_0 \approx 0.4$ kg)	Parrot Bebop		
	TrueXS Racing UAS		

For the MBS model of the Hypothetical stiff UAS, the base model of DJI Phantom III is used but modified into a single lumped mass with a rigid body mass concentrated in the centre of the fuselage and cutting out all other flexible components. The Tarot LJI500 and DJI F450 MBS models share a similar model structure to DJI Phantom III, with landing gears modelled. Since they are customizable UASs, the camera gimbal is not already installed, as seen in the real-world system in Table 2. However, they both have camera gimbal options similar to those of DJI Phantom III. Therefore, both DJI F450 and Tarot LJI500 use the same camera gimbal MBS model as DJI Phantom III. For Parrot Bebop and TrueXS Racing, UAS MBS models consist simply of a main fuselage and motor arms similar to those of their real-world system.

Similarly to DJI Phantom III, the MBS views of the four additional UAS types are translated into a network of rigid bodies, kinematic joints, and force restraints. Ellipsoid surfaces are attached to these bodies to realistically represent the model's external geometry and are used for contact modelling. For the Hypothetical UAS, there are no joints and there is only one rigid body. Figures 1–6 show the construction of the MBS model for each of the five UAS types, respectively. Bodies, joints and restraints highlighted in the colour red, shown in Figures 3 and 4, represent the new parts that are extended relative to the MBS model of DJI Phantom III in Figure 1.
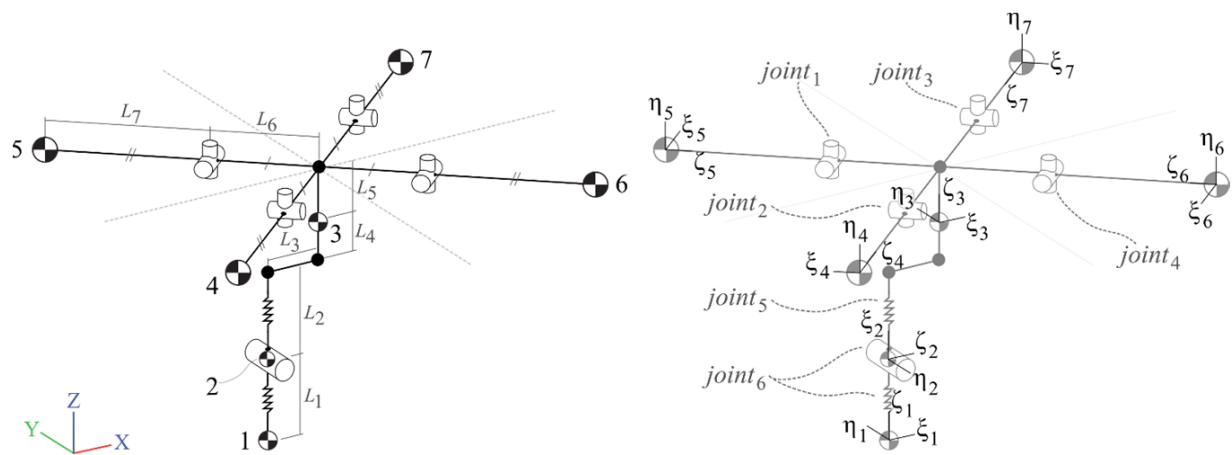
Figure 1. Skeletons of DJI Phantom III UAS multibody system model. This MBS model was developed in [27]. The symbols in the left-hand figure have the following meanings: the numbers 1–7 are coupled to the 7 parts with a non-zero mass, and *L*x is the length of segment x; the Greek symbols ξi, ηi, and ζi in the right-hand figure represent the local orthogonal coordinate axes for body *i*, where *i* = 1, 2, . . ., 7.
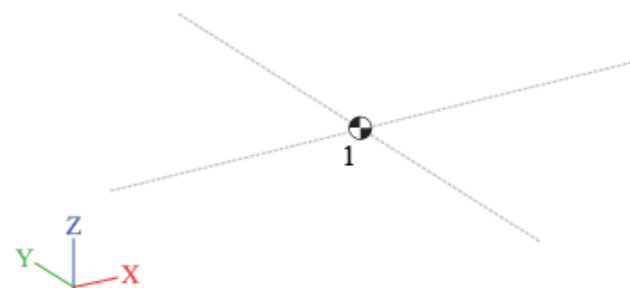
Figure 2. Skeletons of Hypothetical UAS multibody system model; it has no joints and only one single rigid body (reproduced from [28]).
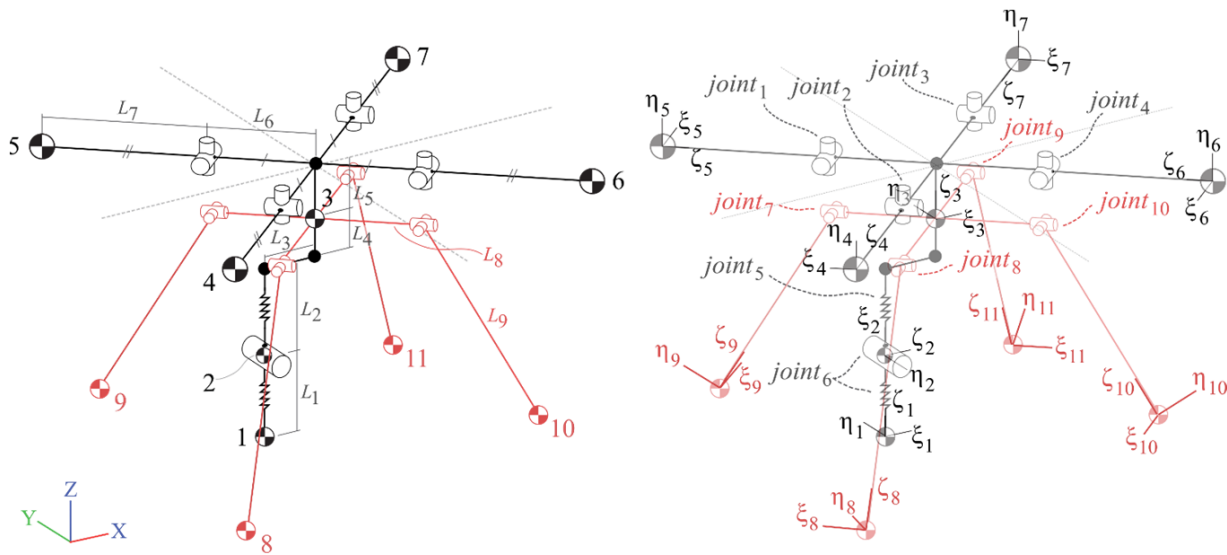
Figure 3. Skeletons of DJI F450 UAS multibody system model. The body, joint and restraint highlighted in red show the parts extended from the baseline model (reproduced from [28]).
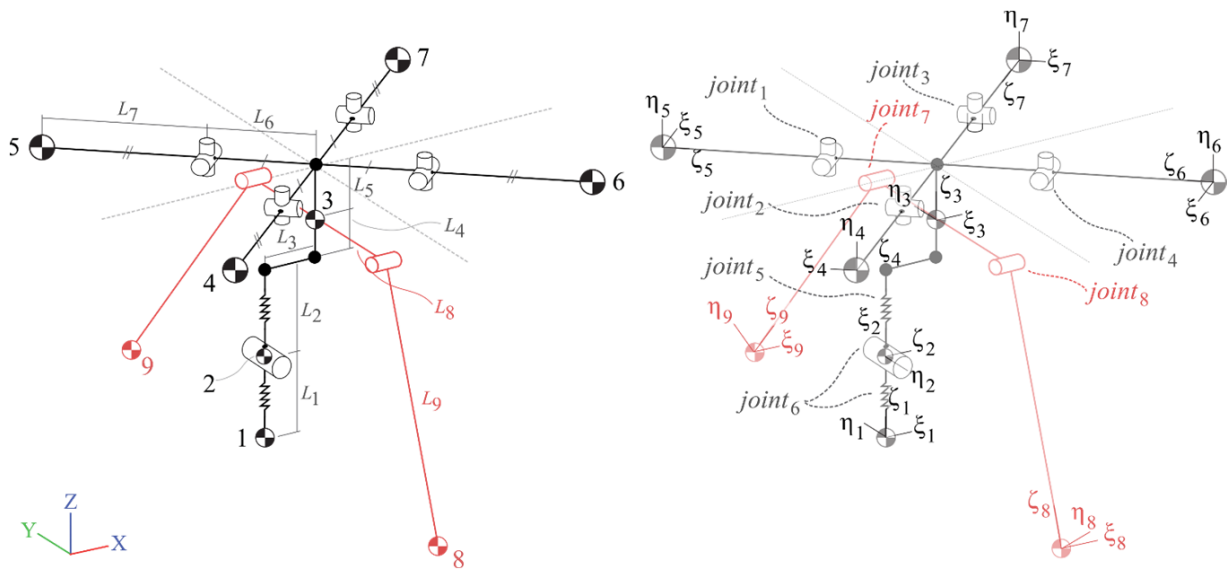
Figure 4. Skeletons of Tarot LJI500 UAS multibody system model. The body, joint and restraint highlighted in red show the parts extended from the baseline model (reproduced from [28]).
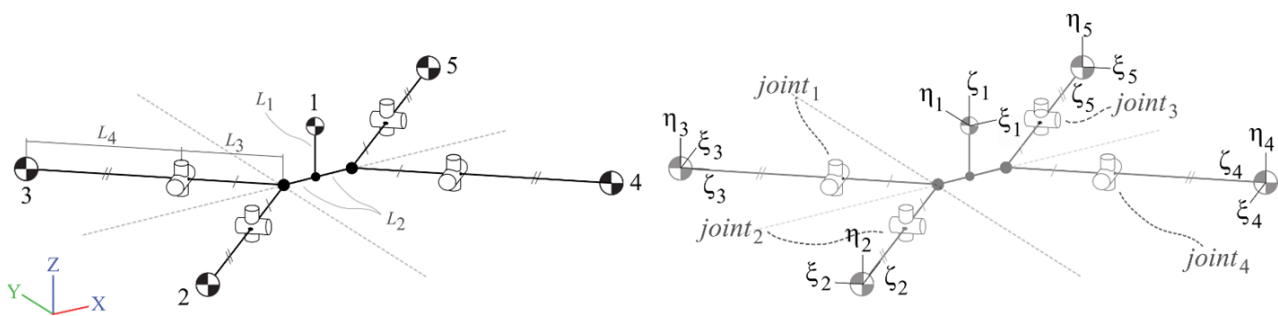
Figure 5. Skeletons of Parrot Bebop UAS multibody system model (reproduced from [28]).
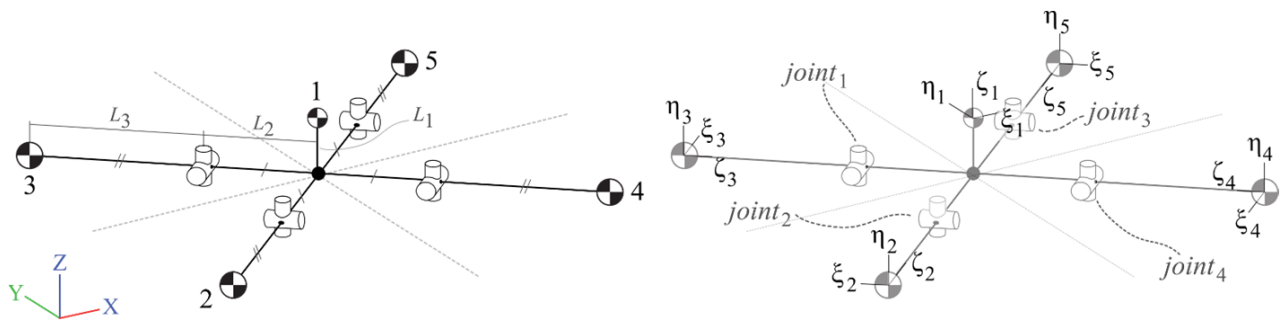
Figure 6. Skeletons of TrueXS Racing UAS multibody system model (reproduced from [28]).

Table 3 shows the measured segment body masses and the segment sizes. The mass and size of each segment body are obtained using a digital weight scale and via size measurements of the corresponding physical segment from the real system.

Table 3. Mass and sizes of the MBS-modelled segments for the five + one UAS models.

| UAS Model	Segment Body Masses [kg]	Segment Lengths [m]
DJI Phantom III (Baseline)	$W_1 = 0.101$, $W_2 = 0.056$, $W_3 = 0.839$, $W_{4-7} = 0.055$	$l_1 = 0.040$, $l_2 = 0.020$, $l_3 = 0.023$, $l_4 = 0.016$, $l_5 = 0.030$, $l_6 = 0.014$, $l_7 = 0.165$
Hypothetical UAS (Rigid)	$W_1 = 1.21$	-
DJI F450	$W_1 = 0.101$, $W_2 = 0.056$, $W_3 = 0.640$, $W_{4-7} = 0.087$, $W_{8-11} = 0.017$	$l_1 = 0.040$, $l_2 = 0.020$, $l_3 = 0.023$, $l_4 = 0.020$, $l_5 = 0.008$, $l_6 = 0.030$, $l_7 = 0.170$, $l_8 = 0.049$, $l_9 = 0.100$
TarotLJI500	$W_1 = 0.101$, $W_2 = 0.056$, $W_3 = 0.621$, $W_{4-7} = 0.090$, $W_{8-9} = 0.040$	$l_1 = 0.040$, $l_2 = 0.020$, $l_3 = 0.023$, $l_4 = 0.020$, $l_5 = 0.008$, $l_6 = 0.030$, $l_7 = 0.170$, $l_8 = 0.060$, $l_9 = 0.200$
Parrot Bebop	$W_1 = 0.360$, $W_{2-5} = 0.010$	$l_1 = 0.015$, $l_2 = 0.025$, $l_3 = 0.055$, $l_4 = 0.080$
TrueXS Racing UAS	$W_1 = 0.360$, $W_{2-5} = 0.010$	$l_1 = 0.012$, $l_2 = 0.032$, $l_3 = 0.080$

2.3. Joint Types and Force/Moment Characteristics

Structural deformation is modelled using various joint types connecting the body segments with Translational and rotational degrees of freedom (DoF). For each joint, applicable restraint force and moment characteristics shall be defined. Table 4 shows which force and moment characteristics have been measured for each UAS joint using quasi-static compressive tests on each part of the UAS. To derive the mechanical properties, experimental data from quasi-static compression and ground vibration tests (GVT) were processed systematically. Raw force–displacement and moment–angular displacement measurements from the compression tests were smoothed using polynomial regression and spline fitting techniques to extract accurate stiffness and damping values for each joint type. Hysteresis curves were generated to capture energy dissipation characteristics under cyclic loading. In parallel, GVT was conducted to identify the natural frequencies of key structural components. The measured frequencies were used to calibrate damping coefficients by ensuring consistency between observed modal behaviour and simulated dynamic responses. These processed mechanical parameters were then implemented within the MADYMO MBS framework, providing a physically grounded representation of structural compliance and dynamic force transmission during UAS–human impact simulations. The details of these tests are explained in various steps in [27]. The measured moment–angular displacement and force–displacement curves are shown in Figures 7 and 8, respectively. These measured curves form the input to the MBS models in MADYMO.
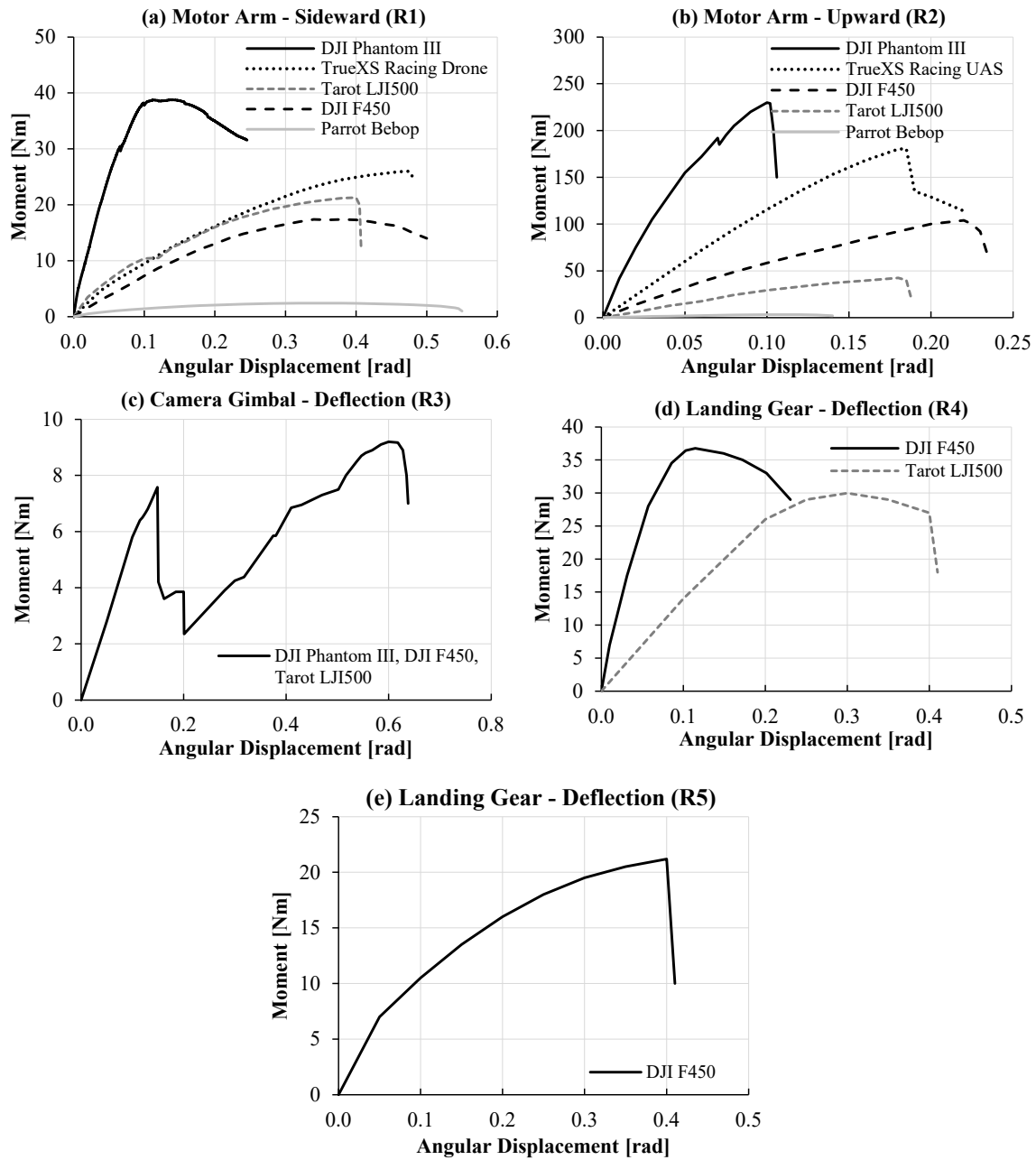
Figure 7. Measured moment characteristics R1 to R5 (reproduced from [28]).
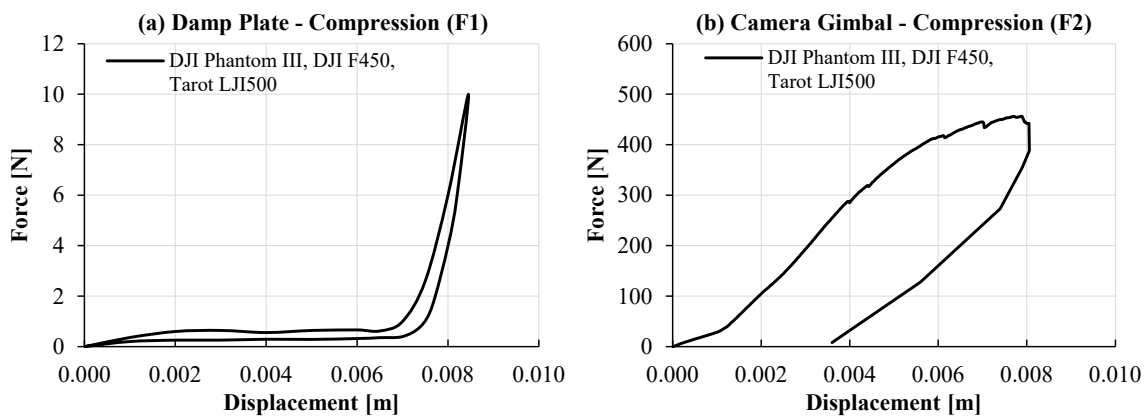

Figure 8. Measured hysteresis loop of force characteristics F1 and F2, which apply for DJI Phantom III, DJI F450 and Tarot LJI500 (reproduced from [28]).

Table 4. Joint types used in each UAS MBS model, and applicable moment/force characteristics for each joint. Measurements of moment characteristics R1–R5 are given in Figure 7a–e. Measurements of force characteristics F1–F2 are given in Figure 8a,b.

UAS Type	Joint Type	Moment Characteristics	Force Characteristics
DJI Phantom III	Joint 1–4 (Universal)	R1, R2	-
	Joint 5 (Translational)	-	F1
	Joint 6 (Translational–Revolute)	R3	F2
Hypothetical UAS	-	-	-
DJI F450	Joint 1–4 (Universal)	R1, R2	-
	Joint 5 (Translational)	-	F1
	Joint 6 (Translational–Revolute)	R3	F2
	Joint 7–10 (Universal)	R4, R5	-
Tarot LJI500	Joint 1–4 (Universal)	R1, R2	-
	Joint 5 (Translational)	-	F1
	Joint 6 (Translational–Revolute)	R3	F2
	Joint 7–8 (Revolute)	R4	-
Parrot Bebop	Joint 1–4 (Universal)	R1, R2	-
TrueXS Racing UAS	Joint 1–4 (Universal)	R1, R2	-

For DJI Phantom III, Joint 1–4 represent motor arms. The Universal joint type is used for Joint 1–4, providing 2 rotational DoF (upward and sideward deflections). Moment characteristics R1 and R2 are measured for these joints. Joint 5 uses a Translational joint with 1 DoF, to model damping plate motion with force characteristic F1. Camera gimbal Joint 6 is modelled using a Translational–Revolute joint. This joint type provides 1 Translational DoF and 1 rotational DoF. For this joint type, moment characteristics R3 and force characteristics F2 are measured. Because the Hypothetical UAS is a rigid-body version of DJI Phantom III, no additional measurements are needed.

DJI F450 motor arms are also modelled using a Universal joint type with moment characteristics R1 and R2 for each joint. DJI F450 uses the same camera gimbal as DJI Phantom III. This makes Joint 5 and Joint 6, along with their moment/force characteristics, identical to those of DJI Phantom III. An additional four landing gears in DJI F450 are modelled using Universal Joint 7 to 10 with moment characteristics R4 and R5 measured on each DoF.

For Tarot LJI500, motor arms are modelled using Universal Joint 1–4 with moment characteristics R1 and R2 measured for each joint. The camera gimbal is identical to that of DJI Phantom III. An additional extension of two landing gears attached to the fuselage is modelled with revolute Joint 7 and 8. Both joints use moment characteristics R4 and R5 on each DoF.

The Bebop and TrueXS Racing UAS MBS models are simply made up of fuselage and 4 motor arms. The 4 motor arms are modelled using Universal Joint 1–4. Moment characteristics R1 and R2 are measured for all 4 joints.

2.4. Contact Characteristics

Contact characteristics between a UAS and human head are modelled for different parts of the UAS as shown in Figure 9 using an analytical elastic–perfectly inelastic contact model [29]. There are four types of contact characteristics used in the model. Locations

of these four contact types are illustrated in the MBS views in the right column of Table 2. These contact types differ due to the difference in materials and geometrical properties of the two contact bodies. 'Camera Bottom Contact' and 'Camera Front Contact' are for the camera gimbal and human head scalp where the gimbal materials are aluminum. The difference between 'Camera Bottom Contact' and 'Camera Front Contact' is the contact radius. 'Camera Bottom Contact' is for the bottom of the gimbal where the surface area is large and Camera Front Contact is for the circular front part of the camera with a small contact radius. 'Fuselage/Motor Arm Contact' represents the contact characteristics between the plastic and human head scalp—this applies to the fuselage, motor arms and landing gears. Lastly, 'Bebop Front Fuselage Contact' is the contact between a polystyrene part of Parrot Bebop and the human scalp.
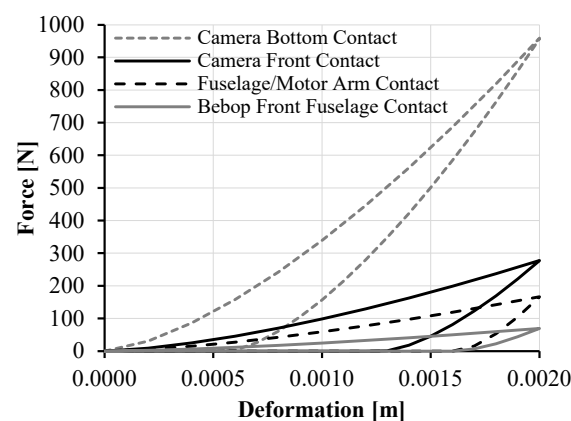
Figure 9. UAS contact type characteristics derived from an analytic contact model [29]. Note that each curve consists of loading and unloading parts which form a hysteresis loop. Contact types 1 and 2 differ in contact radius (reproduced from [28]).

2.5. MBS Model of Human Body and Head Injury

The assessment of the effect of different UAS types on human head injury is performed using the UAS MBS models shown in Table 2 and the 50% percentile male body model within MADYMO [30,31]. The biofidelic human body model [16] is a validated multibody system model that is representative of the mid-size German adult male. Non-linear models capture joint resistance in terms of rotational and Translational stiffness and damping, lumping the effects of passive joint compliance and muscular stabilization. The skin is made up of a mesh of shell-type massless contact elements. The biomechanical data including joint characteristics and mechanical properties are based on biomechanical data and are validated using volunteer and post mortem human subjects (PMHS) [31]. Although this model was originally defined and validated for seated postures, the hip joints also allow for straightforward application to the standing posture.

MBS simulation of the UAS impact on the human head involves impact parameters that are shown in Figure 10, i.e., impact velocity (V), head direction (ψ), UAS elevation (θ), and UAS pitch angle (α). The UAS is positioned relative to the human head, with a velocity vector pointing toward the head's CG (centre of gravity). An impact condition for central impact is applied, meaning that the line of action of the impact velocities is collinear and passes through the centres of mass of the two bodies.
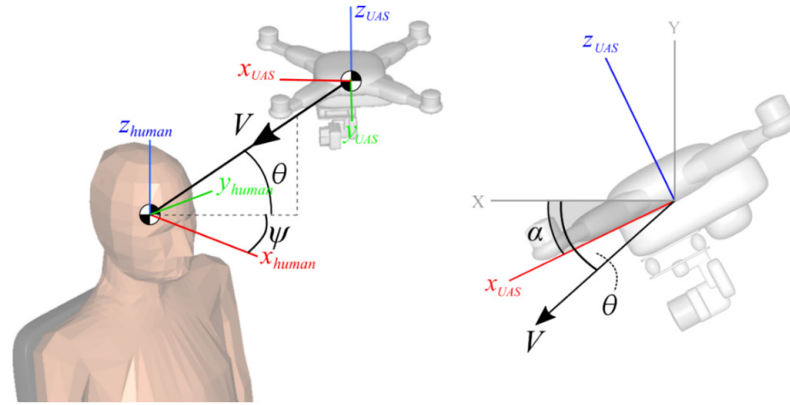
Figure 10. UAs—human head impact simulation setup parameters (reproduced from [28]).

MADYMO supports the measurement of the head injury criterion (HIC_{15}), where the subscript value of 15 refers to the duration in ms of the worst time interval after the first moment of impact. The equation for calculating the HIC value [30] is given as an integral over the head CG (centre of gravity) acceleration:

$$HIC_\Delta = \Delta \max_{T_0 \leq t < t+\Delta \leq T_E} \left[\frac{1}{\Delta} \int_t^{t+\Delta} a(t')dt' \right]^{2.5} \tag{1}$$

where T_0 is the first moment of impact, T_E is the end time of the period considered after the first impact, and $a(t)$ is the acceleration–time curve of the head CG. Based on the Federal Motor Vehicle Safety Standards (FMVSS), an HIC_{15} value of 700 is the minimum safety threshold for non-fatal impact. It should be noted that the HIC_{15} injury criterion is mainly developed for the blunt-force injury type. The limitations of this injury criterion are evident when dealing with impact from an object with a small surface area, where local penetration is more prominent than the impact force transfer over a large surface area.

MADYMO also supports the measurement of the neck injury level in terms of a neck injury criterion N_{ij} that considers the upper neck force and moment originally proposed by the National Highway Traffic Safety Administration (NHTSA) [32]. This formulation laid the foundation for pediatric injury reference values, which were validated by Arbogast et al. [33] and further refined in [34,35]. This criterion is designed for frontal-collision injury evaluation in automotive accidents. "ij" represents indices for the 4 injury mechanisms, namely N_{TE}, N_{TF}, N_{CE}, and N_{CF}. The first index, j, represents the actual load (tension or compression) while the second index j represents the sagittal plane bending moment (neck flexion or extension). The equation for N_{ij} is as follows:

$$N_{ij} = \left| \frac{F_{Z,i}}{F_{\text{int},i}} \right| + \left| \frac{M_{Y,j}}{M_{\text{int},j}} \right| \tag{2}$$

where $F_{Z,i}$ is the upper neck force about the Z axis, $F_{int,i}$ is the threshold force, $M_{Y,j}$ is the upper neck moment about the Y axis and $M_{int,j}$ is the threshold moment. The current performance limit of N_{ij} is 1, which represents 22% of $p(AIS \geq 3)$ [36], which can be described as multiple nerve root lacerations in the cervical thoracic spine [37]. The equation converting N_{ij} into $p(AIS \geq 3)$ is as follows:

$$p(AIS \geq 3) = \frac{1}{1 + e^{3.227 - 1.969 N_{ij}}} \tag{3}$$

2.6. Conversion into Probability of Fatality

To assess the probability of life-threatening injuries due to the UAS impact on a human head, a conversion curve of HIC_{15} in probability of fatality (PoF) is adopted. Figure 11 illustrates the adopted curve from the U.S. ISO delegation [38], which is based on Prasad and Mertz's injury risk curve [39]. This curve allows for the conversion of the HIC_{15} level measured in the MBS simulations into the PoF value.
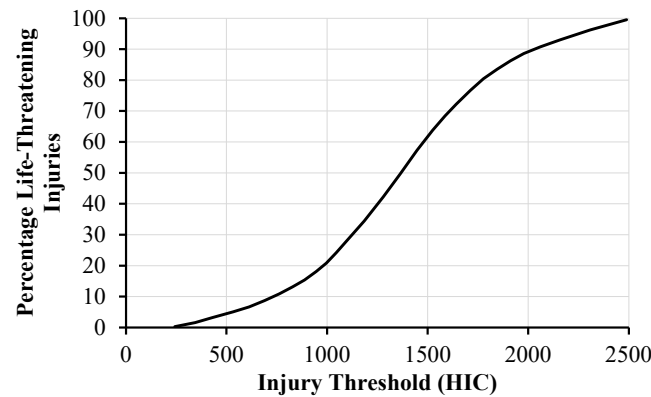
Figure 11. Conversion of HIC15 level into the percentage of life-threatening injuries recommended by U.S. ISO delegation [38], derived from Prasad and Mertz's injury risk curve [39].

3. Impact Scenario Selection and Simulation Setup

Two UAS impact scenarios will be simulated with the MBS model in MADYMO: controlled horizontal flight impact and uncontrolled vertical drop impact. The relevance and details of these two scenarios are described in Sections 3.1 and 3.2, respectively.

3.1. Controlled Horizontal Flight Impact

Under controlled horizontal flight, a UAS is capable of reaching a maximum designed operational speed. This is particularly interesting since it yields the highest possible impact energy for each of the UAS types. This impact scenario can occur when, for example, a loss of link between the UAS and operator takes place, which makes the UAS continue flying in a controlled manner under an autopilot system. Without manual control override from an operator or an automatic safety cutoff, the UAS will continue its original course and may accidentally hit a person nearby. This scenario may also arise from pilots accidentally flying the UAS too close to nearby bystanders and failing to react to avoid a collision, leading to an impact on a human at full operational speed. This is particularly relevant to racing UAS, where flight altitude is close to ground level and close to bystanders.

For controlled horizontal flight, the encounter setup is shown in Figure 12. For this scenario, it is of interest to look at the parameter setup that results in the worst impact. DJI Phantom III's impact on the side (ψ = 90°) of the human head results in the worst impact case [40]. Therefore, head direction (ψ) is set to 90°. Impact elevation is set to 0° since only horizontal impact is considered. In reality, at full maximum operational velocity, UAS has to pitch downward with a small angle in order to produce a forward thrust force. Nevertheless, this angle is rather small and is neglected in the simulation. Hence, the UAS pitch angle is set to 0°.
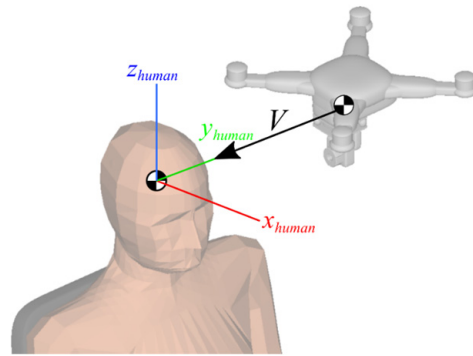
Figure 12. Controlled horizontal flight encounter scenario, i.e., $\psi = 90°$, $\theta = 0°$, and $\alpha = 0°$. The maximum impact speed is 48 m/s for TrueXS Racing, 16 m/s for Parrot Bebop, and 18 m/s for the other UAS types (reproduced from [28]).

Furthermore, for DJI Phantom III, the maximum attainable speed is up to 18 m/s. DJI F450 and Tarot do not have specific maximum operational speeds due to their customizability. However, since they are similar in size and weight to to DJI Phantom III, it is assumed that their maximum operational speed is equal to that of DJI Phantom III. For the Hypothetical UAS, the maximum attainable speed is 18 m/s, similar to that of DJI Phantom III. Bebop's maximum operational speed is 16 m/s based on the manufacturing data [41].

Lastly, the TrueXS Racing UAS also does not have a specific maximum operational speed due to its customizability. Therefore, an average maximum operational speed of 48 m/s, compiled from 14 racing UASs, is used [42]. Hence, the simulated impact speed of each UAS is set from 0 m/s to the maximum operational speed in 2 m/s increments.

3.2. Uncontrolled Vertical Drop Impact

The second impact scenario chosen is uncontrolled vertical drop, shown in Figure 13, at an impact speed $V = 18$ m/s. This case may occur due to loss of control [43], which may be caused by partial or complete propulsion failure, control system failure, the UAS entering an unstable wake region outside of its operational envelope, etc. This scenario applies to many urban UAS operations, such as aerial photography over crowds or parcel delivery in a populated area. A UAS falling vertically downward on a pedestrian is deemed to be a critical case since the UAS can reach a terminal speed, and the pedestrian may not be aware of the falling UAS, making self-protection impossible.
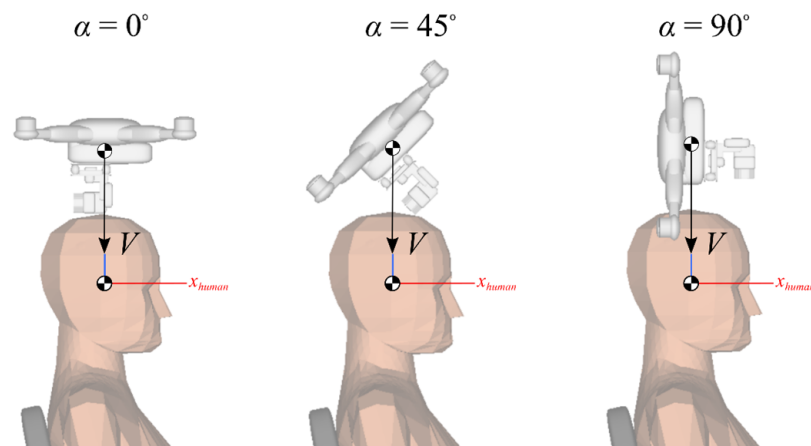
Figure 13. Encounter scenario for vertical drop impact cases, i.e., $\psi = 0°$ and $\theta = 90°$; the three pitch angle values, $\alpha = 0°$, $\alpha = 45°$ and $\alpha = 90°$ (left to right); and the impact speed, $V = 18$ m/s (reproduced from [28]).

Because UASs under such flight conditions typically tumble down towards the ground [44], the impact geometry may vary. To capture this, three sub-scenarios are evaluated for different UAS pitch angle values of 0°, 45° and 90°, as is shown in Figure 13. In the 0° pitch angle configuration, the UAS bottom surface impacts the top of the head, representing a flat-body collision. At 45°, a corner or arm strikes the head at an oblique angle, leading to partial rotation and a mix of Translational and angular force transfer. The 90° pitch angle simulates a frontal fuselage strike, which tends to concentrate force in a smaller area and aligns the impact force vector with the cervical spine, making it a worst-case scenario for axial loading.

Furthermore, since the UAS drop freely towards the ground in this scenario, it is assumed that the maximum impact velocity that can be achieved by the UAS is its terminal velocity. ASSURE [17,45] estimated DJI Phantom III's terminal velocity to be approximately 18 m/s by using a computational fluid dynamics model to determine the aerodynamic force acting on the UAS. Because the DJI F450, Tarot LJI500 and Hypothetical UASs are of similar sizes and weights, it is assumed that the terminal velocity of these UASs is equal to that of DJI Phantom III. With regards to the Parrot Bebop and TrueXS Racing UASs, because these UASs have a much lighter weight than DJI Phantom III, it is possible that their terminal velocity may be lower. Nevertheless, it is of interest to use the terminal drop velocity of DJI Phantom III as it can represent a possible upper-bound terminal drop velocity for the Tarot LJI500 and TrueXS Racing UASs.

Based on the scenarios for the uncontrolled vertical drop scenario, the impact attitude of each UAS is shown in Figure 14. The figure illustrates the different points of contact for each UAS on the human head at different pitch angles.
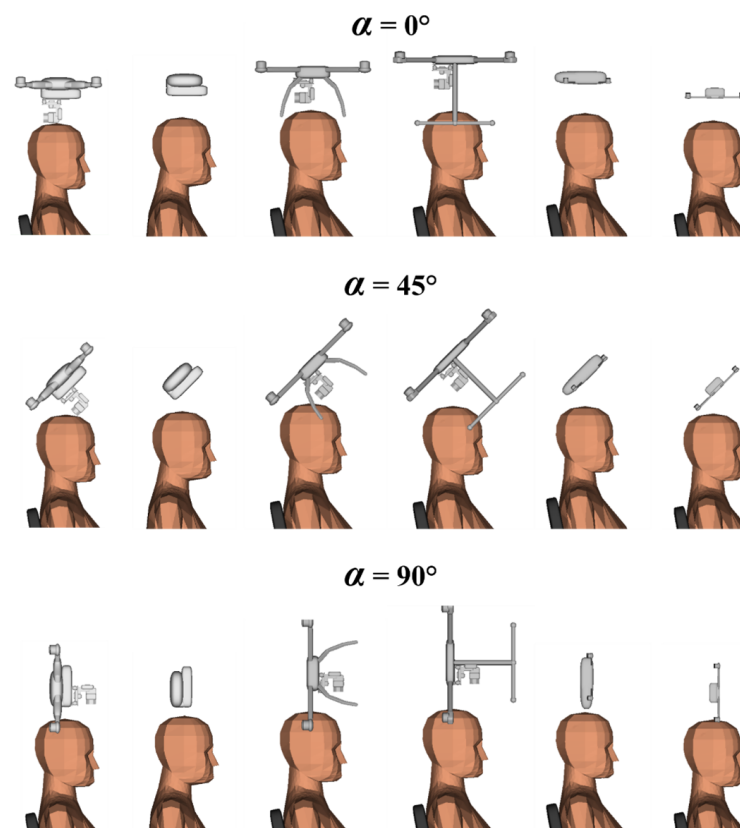
Figure 14. Visualization of vertical drop scenario of Figure 13 for each of the five + one MBS models under pitch angles of 0, 45 and 90 degrees (reproduced from [28]).

As has been explained in Section 2.2, the MBS model of DJI Phantom II is without landing gear; hence, landing gear is also missing in the left-side sub-figures in Figure 14. If landing gear was included in these conditions, then the following would happen: for $\alpha = 0°$, the left and right landing gears would pass the head sideways, and therefore would have zero effect; for $\alpha = 90°$, the landing gear would also avoid hitting the head, and therefore would also have zero effect; for $\alpha = 45°$, one side of the landing gear would hit the head first, and would then flexibly bend, as a result of which there would be a minor effect only on the impact geometry and the impact speed.

4. Simulation Results for Controlled Horizontal Flight Impact

In this section, the MADYMO-integrated MBS models are used to simulate controlled horizontal impacts for the Hypothetical UAS, DJI Phantom III, Tarot LJI500, TrueXS Racing UAS, DJI F450 and Parrot Bebop. Section 4.1 presents the head CG acceleration time history results. Section 4.2 presents the head injury criterion (HIC_{15}) results. Section 4.3 presents the neck injury criterion (N_{ij}) results. Section 4.4 presents the probability of fatality (PoF) results. Section 4.5 compares and discusses the results obtained for the different UAS types.

4.1. Head CG Acceleration–Time History

As is expressed in Equation (1), head acceleration over time forms the inputs for HIC_{15} assessment. Hence, head acceleration curves were simulated for each UAS type in various impact conditions. For the impact conditions of maximum impact energy, Figure 15 shows the head CG acceleration–time history of the human head, starting from the initial contact moment, for each UAS type.
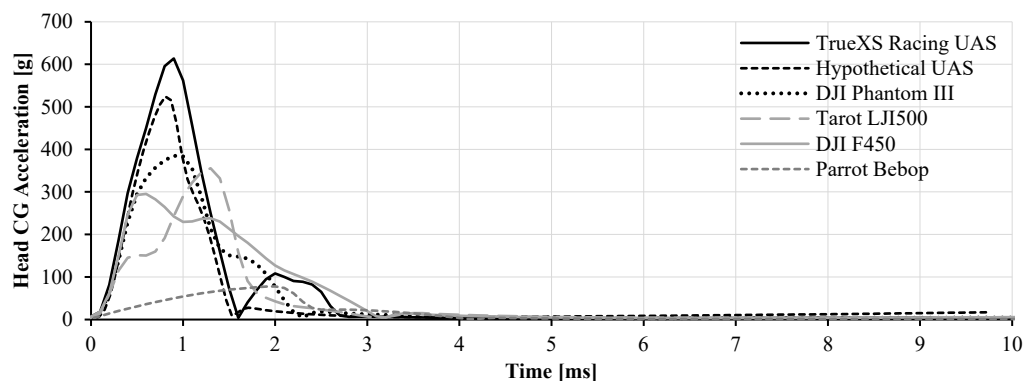
Figure 15. Head CG acceleration time–history curves at the maximum impact energy of each UAS type (reproduced from [28]).

Figure 15 shows that the TrueXS Racing UAS has the highest peak acceleration of 614 g within 1 ms. The Hypothetical UAS reaches its peak value of 500 g at approximately 0.9 ms. DJI Phantom III reaches its peak value of 400 g at 1 ms. Tarot has a relatively high peak of 330 g, which is reached at about 1.5 ms. It is observed that the Tarot UAS has a small sharp rise in head acceleration at 0.5 ms, followed by a flat region for a very short period before peak acceleration is reached.

DJI F450 induces lower head acceleration with a peak value of 283 g at 0.7 ms. DJI F450 has a similar compression rate compared to DJI Phantom III, but with a slower rebound rate as the downslope is much less steep. Bebop yields a significantly lower peak head acceleration of only 74 g at 1.8 ms. This shows that the Parrot Bebop UAS' compressive phase is much slower than that of other UAS types.

4.2. Head Injury Criterion (HIC₁₅)

The simulated head CG acceleration–time histories are used as input for Equation (1) to assess the resulting head injury criterion (HIC_{15}) for each of the UAS types under various conditions. The obtained HIC_{15} results are presented in Figure 16 as a function of increasing impact energy for each of the five UAS types. The curves show that the HIC_{15} level increases non-linearly with impact energy. Serious and critical head injuries (i.e., $HIC_{15} > 700$) have been obtained for all UAS types, with the exception of Parrot Bebop. The human head sustains low injury from Parrot Bebop's impact, with the highest HIC_{15} being only 52.
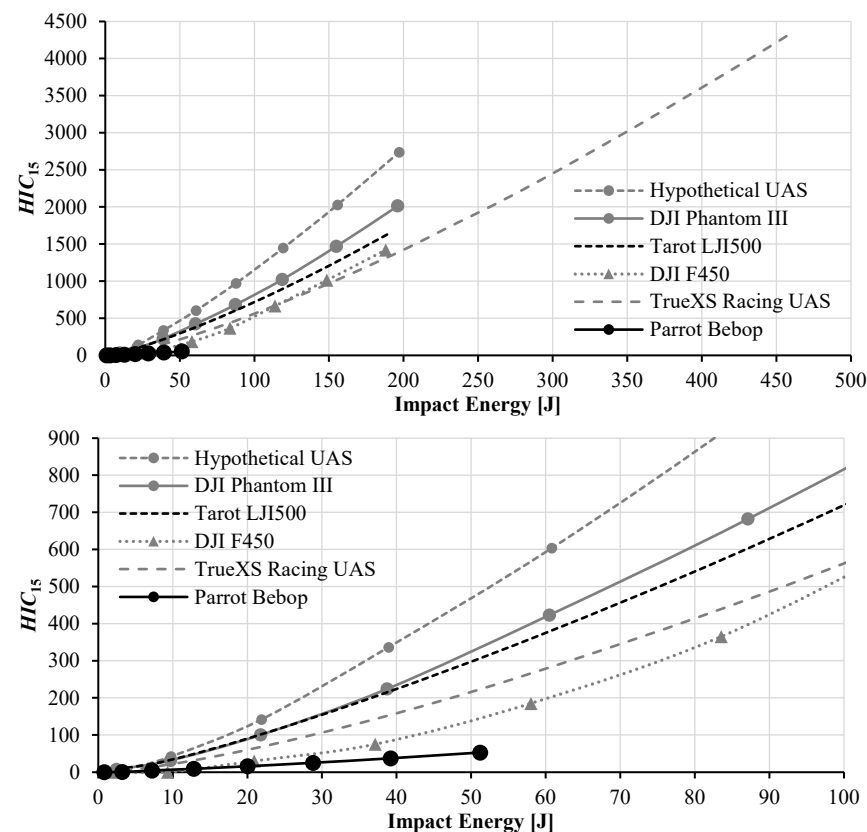
Figure 16. HIC_{15} results for controlled horizontal flight impact, with the bottom figure zooming in on the low HIC_{15} and impact energy range (reproduced from [28]).

The Hypothetical UAS produces the steepest HIC_{15} curve [29]. DJI Phantom III has the next steepest HIC_{15} curve. Tarot LJI500 has the third steepest HIC_{15} curve. The fourth and fifth steepest HIC_{15} curves belong to DJI F450 and TrueXS Racing UAS, respectively. Parrot Bebop has the lowest slope for the HIC_{15} curve, and stops at 52 J. For TrueXS Racing, the HIC_{15} curve continues for kinetic energy values above 200 J.

4.3. Neck Injury (N₍ᵢⱼ₎)

In addition to head injury, the neck injury level on the human body due to UAS impact is assessed using the neck injury criterion (N_{ij}). Figure 17 shows the N_{ij} results at different impact energies for different UAS types. For all UAS types, N_{ij} values indicate non-critical neck injury. The highest N_{ij} observed is 0.401, which is inflicted by the TrueXS Racing UAS. This N_{ij} level is equivalent to a 8.2% risk of moderate neck injury (AIS $\geq$ 3). Even the TrueXS Racing UAS, which inflicts a life-threatening HIC_{15} level, does not inflict serious neck injury, with a maximum N_{ij} level of less than 0.48 (9.3% of $p(\text{AIS} \geq 3)$)
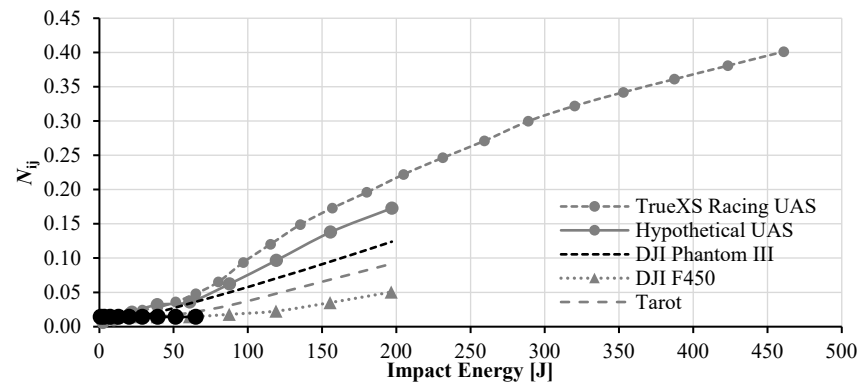
Figure 17. Neck injury from horizontal/side impact (reproduced from [28]).

4.4. Probability of Fatality (PoF)

The next step is to transform the neck and head injury assessments into probability of fatality (PoF) results. Because neck injuries have been shown to be negligible compared to head injuries, the HIC_{15} values only need to be transformed into PoF values. As is analyzed in Appendix A, based on the PHMS impact test results from Ohio State University [22], our MBS simulation tends to underestimate the HIC_{15} level by 11%. Taking into account the variation in PMHS sizes and weights in the live test scenarios, this 11% difference is remarkably small. Nevertheless, this finding is used to compensate for the MBS-assessed HIC_{15} curves in Figure 16 as follows: prior to using the conversion curve in Figure 11, the HIC_{15} curves in Figure 16 are increased by a factor 1.11; the combination of these two conversions yields the PoF curves in Figure 18 as a function of impact energy, with one for each UAS type. The sequence of these curves is similar to the sequence found for the HIC_{15} curves in Figure 16.
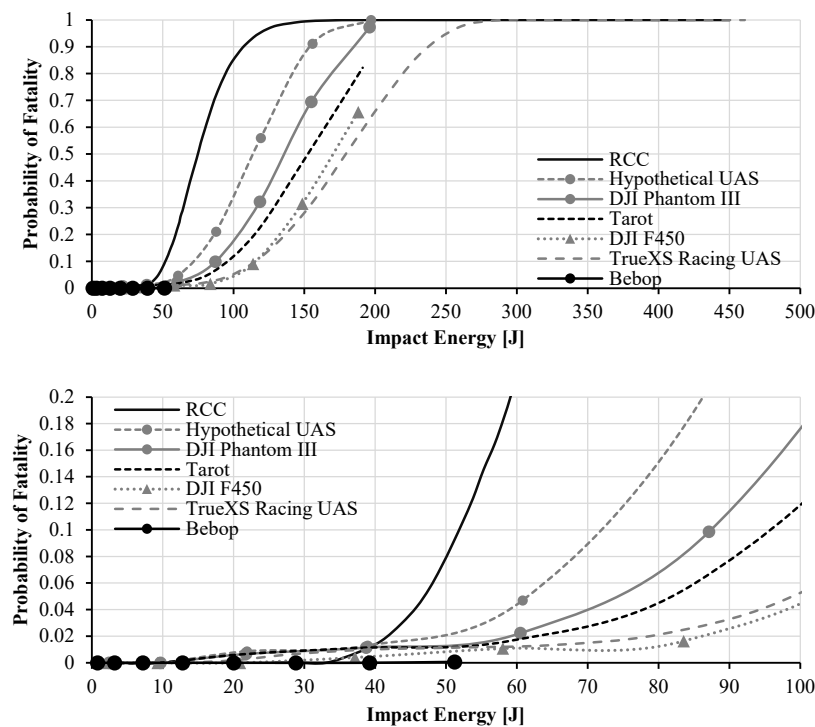
Figure 18. Probability of fatality (PoF) as a function of impact energy in the case of horizontal impact by each of the five UAS types and the corresponding curve from RCC [13]. The PoF curves are converted from the HIC_{15} curves that have been compensated for in terms of the +11% systematic underestimation. The bottom figure zooms in on the low HIC_{15} and impact energy range (reproduced from [28]).

For reference purposes, Figure 18 also shows the widely adopted Range Commanders Council (RCC) curve for head injury [13]. In order of PoF severity, the RCC curve ranks first. The RCC curve shows an increase with impact energy and resembles an S-shape curve as impact energy increases with a plateau value of 1. The PoF curve of the Hypothetical UAS stays well behind the RCC curve. The curve of the Hypothetical UAS is lower by approximately 80% in the range of 100 J to 150 J. This shows that the RCC curve overestimates the PoF level of humans under UAS collisions. As found in previous work [40], the RCC curve is derived based on small debris explosive data. Hence, it is a representation of blast wave injury [46] or laceration and penetration injury, while UAS impacts are mostly caused blunt-force trauma injury.

4.5. Discussion of Results Relative to UAS Design

The next step is to relate the differences in HIC_{15} and PoF to differences in the airframe design and materials used. The preparatory step in accomplishing this is to compare the HIC_{15} and PoF values of the different UAS types under the same kinetic energy impact level, including a comparison to the RCC curve. In Table 5, such a comparison is made for the RCC model and for each of the UAS types under horizontal impacts at kinetic energies of 151 J (case a) and 51 J (case b).

Table 5. Comparison of HIC_{15} and PoF values for horizontal impacts at 151 and 51 J impact energies. The 2nd and 5th columns specify the impact speed for each UAS type.

Kinetic Energy	151 J (Case a)			51 J (Case b)		
	Speed [m/s]	HIC_{15}	PoF	Speed [m/s]	HIC_{15}	PoF
RCC [13]	n.a.	n.a.	0.99	n.a.	n.a.	0.089
Hypothetical	15.8	1950	0.91	9.2	481	0.022
DJI Phantom III	15.8	1572	0.66	9.2	374	0.022
Tarot LJI500	16.0	1354	0.48	9.3	340	0.011
DJI F450	16.1	1152	0.32	9.4	161	0.010
True XS Racing	27.5	1060	0.30	16	247	0.011
Parrot Bebop	27.5	n.a.	n.a.	16	58	0.001

For a kinetic impact energy of 151 J (case a), the results in Table 5 show several important relations. First, the Hypothetical UAS has a PoF value of 0.91, while the PoF value predicted by the RCC parametric model is 0.99. Second, for DJI Phantom III, the PoF value further reduces by 2/3 times the RCC's PoF value. Third, for the four UAS types (DJI Phantom III, Tarot LJI500, DJI F450, and True XS Racing), their HIC_{15} values differ by a factor of 1.5 (=1572/1060), and their PoF values differ by a factor of 2.2 (=0.66/0.30). Fourth, the differences in HIC_{15} and PoF for these four UAS types reflect differences in their airframe structure and materials. Below, an explanation is given for the relation between design differences in each of these four UAS types and their HIC_{15} values for case a in Table 5.

For case a in Table 5, DJI Phantom III has a 20% lower HIC_{15} value compared to the Hypothetical UAS. The differences in head acceleration curves are also in good agreement with this HIC_{15} difference. For DJI Phantom III, the peak is reached later than for the Hypothetical UAS. This is due to the slower transfer of impact energy to the human head, because DJI Phantom III has flexible components.

For Tarot LJI500, the HIC_{15} value is an extra 14% lower than that for DJI Phantom III. This lower HIC_{15} value is also reflected by a small change in the head acceleration curve in Figure 15, where the peak acceleration is reached later compared to that of DJI Phantom III. This implies that the slope of the head acceleration curve is slightly lower, which means

that the impact energy transfer is not as abrupt as that of DJI Phantom III. Because the UAS weight, impact velocity and contact stiffness are almost equal, the assessed difference is largely due to differences in the airframe structure (UAS shape and construction). An objective assessment of airframe structure differences is conducted based on the quasi-static compressive test on the airframes in Figure 7a,b. This shows that Tarot LJI500 is almost two times less stiff than DJI Phantom III. This results in a more compliant structure which absorbs and dampens the impact energy during impact. However, this effect is not one to one, because shape and mass distribution also play their roles. For instance, motor arm stiffness, as shown in Figure 7a,b, connects the main mass to the lumped masses of the motor and arm. For both DJI Phantom III and Tarot LJI500, the masses of these four motors and arms are approximately 20% of the total mass. Therefore, the amount of impact energy absorbed by these parts out of the total impact energy is less than what the main body absorbs. This explains why reduced motor arm stiffness has only a limited effect on HIC_{15}. Complementarily to arm stiffness, there are some differences in the shape of the two UAS types that will also have a non-linear effect on HIC_{15}.

For DJI F450, the HIC15 value is 27% lower than that of DJI Phantom III. Although the acceleration curve in Figure 15 for DJI F450 shows a similar initial rise to that for DJI Phantom III, the peak value is lower, and the rebound takes longer. The longer rebound phase indicates a softer and dampened structure where more energy is dissipated. Because the UAS weight, impact velocity, contact stiffness and airframe materials (ABS plastic) are the same, the difference may be due to differences in the airframe design (UAS shape and construction). An objective assessment of airframe materials and construction differences stems from the quasi-static compressive test on the airframes in Figure 7a,b. In these figures, the bending stiffness of the DJI F450 motor arm is almost a factor of 3 less steep than for DJI Phantom III. The likely explanation is that, as described in Table 1, DJI F450 has a sandwich plate structure, which is flexible, whereas DJI Phantom III has a shell structure, which is stiff. However, the significantly less stiff motor arms only result in a 27% reduction in HIC_{15}. This again shows that the relation between structural stiffness and HIC_{15} is not one-to-one; also, shape and mass distribution play their roles. For instance, the motor arm stiffness shown in Figure 7a,b connects the main mass to the lumped masses of the motor and arm. For both DJI Phantom III and DJI F450, the masses of these four motors and arms are approximately 20% of the total mass. Therefore, out of the total impact energy, the amount of impact energy engaged by these parts is less than what the main body absorbs. Also, the partial effect n HIC_{15} reduction can be explained by the reduction in motor arm stiffness. Apart from the difference in arm stiffness there, are further differences in the shape of the two UAS types that will also have a non-linear effect on the HIC_{15} value.

For the TrueXS Racing UAS, the HIC_{15} value is 33% lower than it is for DJI Phantom III. Because of its low weight, the 151 J impact energy is reached at a 1.7 higher impact speed than that for DJI Phantom III. Due to TrueXS's small size, the first point of contact is with the two forward motor arms. Upon impact, these two motor arms deflect outward, acting like a spring/damper system, which increases the impact time. Once the maximum deflection of the motor arms is reached, the remaining energy from the main mass of the fuselage is then transferred to the head. This explains the relatively low HIC_{15} value.

For case b (51 J impact energy), the results in Table 5 show the following relations. First, both the Hypothetical UAS and DJI Phantom III have PoF values that are 12% of the PoF predicted by the RCC parametric model. Second, for the four UAS types (DJI Phantom III, Tarot LJI500, DJI F450, and True XS Racing), the PoF values are in the range of 0.011–0.022. Third, for Parrot Bebop, the PoF value decreases by an order of magnitude to 0.001. Fourth, the differences in HIC_{15} and PoF for the two UAS types weighing ~0.4 kg reflect differences in their airframe structure and materials.

For case b, Parrot Bebop's HIC_{15} value is 58, which is a factor of 4 lower than that for True XS Racing. By considering the head CG acceleration induced by Parrot Bebop in Figure 15, the curve shows a gradual rise in head acceleration which takes almost 2 ms to reach the peak acceleration value. This gradual rise shows that the compressive phase for Bebop takes rather long in comparison to that for True XS Racing UAS. This aligns well with the low moment curves measured for Parrot Bebop in Figure 7a,b. These low moment and force curves reflect that the frontal part of the Parrot Bebop is made of soft polystyrene foam. This reduces the moment and force curves and leads to a longer compression phase, lowering the impact force on the human head.

## 5. Simulation Results for Uncontrolled Vertical Drop Impact

In this section, the MADYMO-integrated MBS models are used to simulate uncontrolled vertical drop impacts for Hypothetical UAS, DJI Phantom III, Tarot LJI500, TrueXS Racing UAS, DJI F450 and Parrot Bebop. In all cases, the impact velocity of the UAS is 18 m/s, which generates an impact energy of 65 J for the two light UAS types, and about 195 J for the other UAS types. Based on earlier MBS simulation results of the same vertical dropping of DJI Phantom III onto a human head [27], the risk of neck injury was found to be negligible compared to that of head injury. Therefore, neck injury results are not presented in this section. Section 5.1 presents the head CG acceleration–time history results. Section 5.2 presents the head injury criterion (HIC_{15}) and PoF results for the UAS types measuring 1.2 kg. Section 5.3 presents the head injury criterion (HIC_{15}) and PoF results for the two UAS types measuring 0.4 kg. Section 5.4 compares and discusses the results obtained for the different UAS types.

5.1. Head CG Acceleration–Time History

Figure 19a–c shows the head CG acceleration–time history of the human head starting from the initial contact moment with the five UAS types at various pitch angles. At a 0° pitch angle, Figure 19a shows that the Hypothetical UAS inflicts the highest head acceleration with a rapid rise to peak acceleration at 400 g within 1 ms. The Racing UAS can induce the highest head acceleration, with a peak value of 200 g at 1 ms. Bebop has a slightly lower peak value of 127 g, reached at 1.4 ms. Also, the Bebop and Racing UAS only have one acceleration peak, while DJI Phantom III, Tarot and DJI F450 have two head acceleration peaks. The first peaks reach approximately 110 g at 0.7 ms. The second peaks reach approximately 125 g at 2.4 ms for DJI Phantom III, and are slightly later at reaching 169 g at 3.1 ms for DJI F450 and Tarot.

For a 45° pitch angle, similar head acceleration responses are observed compared to those for a 0° pitch angle. The Hypothetical UAS also inflicts the highest peak acceleration of 430 at 1 ms. TrueXS Racing UAS and Bebop have slightly lower peak values of 160 at 1 ms and 98 at 2 ms, respectively. DJI Phantom III, DJI F450 and Tarot yield similar acceleration curves as for a 0° pitch angle.

For a 90° pitch angle, the peak acceleration of the Hypothetical UAS is similar that for the cases with a 0° and 45° pitch angle. Head acceleration induced by DJI Phantom III, Tarot, and DJI F450 now increases significantly in the 0° and 45° pitch cases. DJI Phantom III has peak value of 340 g at 1.25 ms. That for Tarot is slightly lower, with peak value of 295 g at 1.25 ms. DJI F450's peak value is reached earlier, at 0.9 ms, with value of 229 g. Head acceleration is also lower for the True XS Racing UAS and Bebop. The TrueXS Racing UAS's peak value of 103 g is reached at 1.9 ms. Bebop reaches peak its head acceleration at 3.5 ms with a value of 17 g.
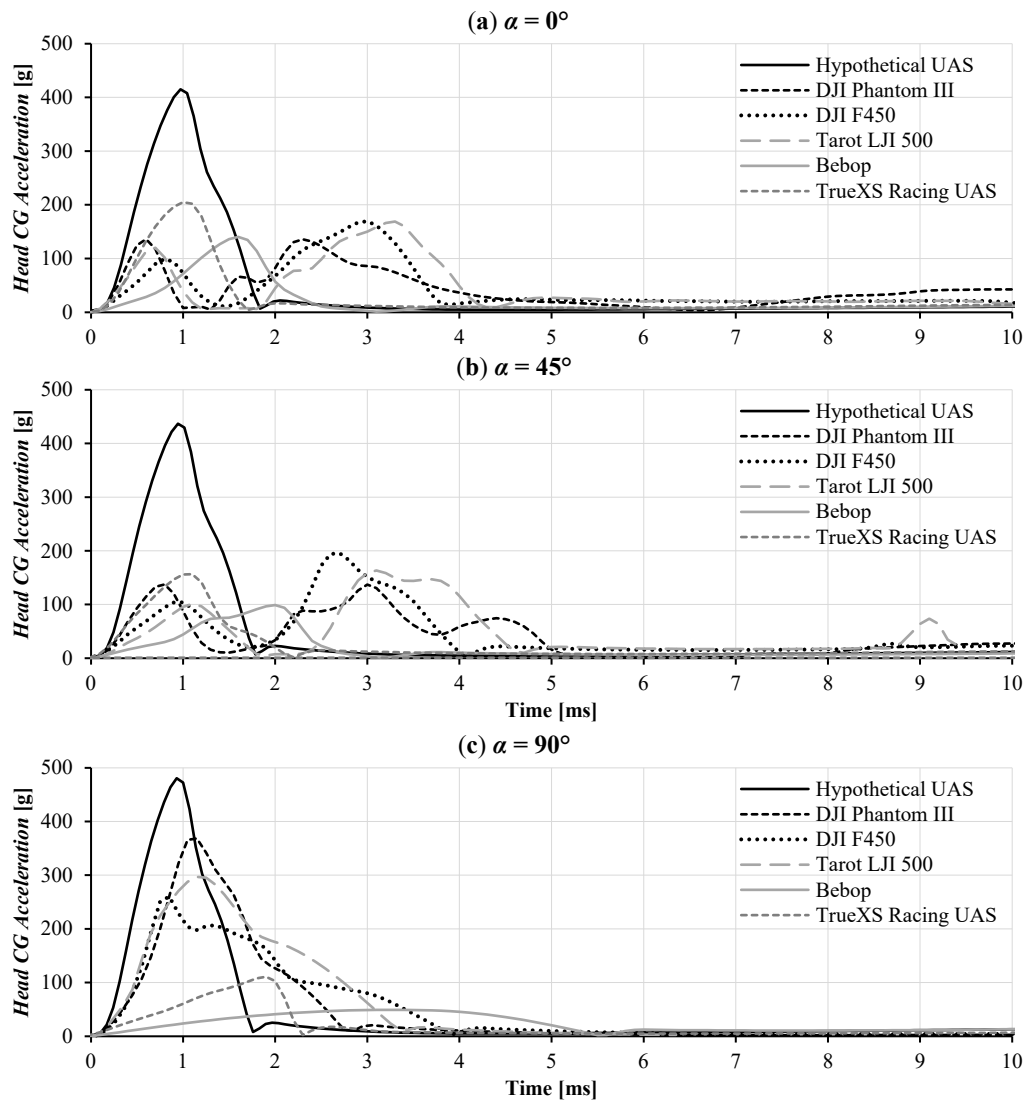
Figure 19. (**a**–**c**) Head CG acceleration time–history for each UAS type at maximum impact energy, for 0°, 45° and 90° pitch angles (reproduced from [28]).

5.2. Head Injury Criterion (HIC$_{15}$) and Probability of Fatality (PoF) for UAS Measuring 1.2 Kg

Table 6 shows the HIC$_{15}$ and PoF results for the 1.2 kg UAS types at a 18 m/s falling speed and at pitches of 90°, 45° and 0° Similarly to the transformation of MBS-based HIC$_{15}$ curves into PoF curves in Section 4.2, HIC$_{15}$ values are multiplied by a factor 1.11 prior to conversion into PoF values. This factor, 1.11, compensates for the 11% systematic underestimation of HIC$_{15}$ by the MBS model; this is analyzed in Appendix A. Note that, in Table 6, for the RCC, no underlying HIC$_{15}$ values are known.

Table 6. HIC$_{15}$ and PoF values for vertical drop impacts for UAS types measuring 1.2 kg, at 0°, 45° and 90° pitch angles.

Pitch Angle	0° (Case a)		45° (Case b)		90° (Case c)	
Unit	HIC$_{15}$	PoF	HIC$_{15}$	PoF	HIC$_{15}$	PoF
RCC [13] 195 J	n.a.	1.0	n.a.	1.0	*n.a.*	1.0
Hypothetical	1502	0.720	1521	0.734	1584	0.778
DJI Ph. III	296	0.013	335	0.014	1239	0.505
Tarot LJI500	272	0.012	291	0.013	982	0.290
DJI F450	173	0.011	201	0.011	800	0.162

For all pitch angles, the RCC model yields a PoF of 1. For a pitch angle of 0° (case a), Table 6 shows that the Hypothetical UAS inflicts the highest HIC_{15} value of 1502, and the second highest PoF value of 0.72. However, DJI Phantom III and Tarot LJI500 inflict 5 times lower HIC_{15} levels of 296 and 272, respectively. DJI F450 inflicts an even lower HIC_{15} value of 173. The resulting PoF values for these three UAS types are 50 times lower than for the Hypothetical UAS, and range between 0.009 and 0.013. The results for a 45° pitch angle, i.e., case b in Table 6, show minor differences compared with those for a 0° pitch angle.

The results for a pitch angle of 90° in Table 6 show much larger variations over different UAS types than those for pitch angles of 0 and 45°. First, the Hypothetical UAS has a PoF value of 0.778, while, the value predicted by the RCC parametric model is 1.0. Second, for DJI Phantom III, the PoF value further reduces to 51% of RCC's PoF value. Third, for the three UAS types (DJI Phantom III, Tarot LJI500, and DJI F450), the HIC_{15} values differ by a factor of 1.5 (=1239/800), and their PoF values differ by a factor of 3 (=0.505/0.162).

The overall view is that differences in UAS design yield a difference of up to a factor of 3 in PoF values. Moreover, the highest of these PoF values is also a factor of 2 lower than the parametric PoF model of the RCC [13].

5.3. Head Injury Criterion (HIC$_{15}$) and Probability of Fatality (PoF) for UAS Measuring 0.4 Kg

Table 7 shows the HIC_{15} and PoF results for the 0.4 kg UAS types at a 18 m/s falling speed and at pitch angles of 0°, 45° and 90°

Table 7. HIC_{15} and PoF values for vertical drop impacts at a speed of 18 m/s for UAS types measuring 0.4 kg, at 0°, 45° and 90° pitch angles.

Pitch Angle	0° (Case a)		45° (Case b)		90° (Case c)	
Unit	HIC_{15}	PoF	HIC_{15}	PoF	HIC_{15}	PoF
RCC [13] 65 J	n.a.	0.32	n.a.	0.32	n.a.	0.32
True XS Rac.	312	0.013	160	0.010	83	0.005
Parrot Bebop	128	0.009	71	0.003	42	0.000

For a pitch angle of 0° (case a), the TrueXS Racing UAS inflicts the highest head injury, with an HIC_{15} value of 312. Bebop inflicts the lowest head injury with HIC_{15} of 128. The resulting PoF values are 0.013 and 0.009, respectively.

For a pitch angle of 45° (case b), TrueXS Racing UAS inflicts an HIC_{15} value of 160, and Bebop inflicts an HIC_{15} value of only 71, and both are about a factor of 2 lower than the value for a 0° pitch angle. The PoF values of the TrueXS Racing UAS and Bebop reduce to 0.010 and 0.003, respectively.

For a pitch angle of 90° (case c), head injury further reduces for Bebop and the TrueXS Racing UAS. This decrease in HIC_{15} leads to very low PoF values: the TrueXS Racing UAS inflicts a PoF of 0.005 and Bebop inflicts a PoF of less than 0.001.

Overall, this means that for the uncontrolled vertical impact of a 0.4 kg UAS at 18 m/s on a model of a human head, differences in the UAS designs considered yield an order of magnitude difference in PoF values. Moreover, the highest PoF value differs by another order of magnitude from the parametric PoF models (RCC) used in standing regulation.

5.4. Discussion of Results Relative to UAS Design

The next step is to relate the differences in HIC_{15} values to differences in the airframe design and materials used. This is performed according to the following sequence:

(i)   The 1.2 kg UAS types at a 90° pitch angle (case c in Table 6);
(ii)   The 0.4 kg UAS types at a 90° pitch angle (case c in Table 7);
(iii)   The 1.2 kg UAS types at a 0–45° pitch angle (cases a, b in Table 6);

(iv)   The 0.4 kg UAS types at a 0–45° pitch angle (cases a, b in Table 7).

Regarding (i), under a 90° pitch angle (case c in Table 6), the UAS hitting geometry in the vertical drop scenario has much in common with case a (high speed) in Table 5 for the horizontal/side impact scenario in Section 4. The main differences are the hitting location on the human head, and a difference of about 45 J in the impact energy for the Hypothetical UAS, DJI Phantom III, TarotLJI500, and DJI F450. A comparison of the Table 5, case a, and Table 6, case c, results for these UAS types shows higher values in Table 5 for the horizontal/side impact scenario. As has been explained in [27], this is due to the biomechanics of the human head and neck complex. Under vertical impact with a 90° pitch angle, there is a significant amount of impact energy being transferred from the head to neck complex. This is because the UAS impact force is vertically aligned with the neck complex's longitudinal axis. On the contrary, in the controlled horizontal case with a 0° pitch angle, the UAS collides horizontally onto the head. There is no body part to absorb the impact force in this lateral direction, making head acceleration 40–60% higher than in the vertical impact case. This also means that the explanation in Section 4.5 of the role played by the airframe and material design also applies for the differences in HIC_{15} values for the different UAS types for case c in Table 6.

Regarding (ii), for True XS Racing and Parrot Bebop at a pitch angle of 90 degrees, the PoF values for case c in Table 7 are even lower than the low values for case b in Table 5 for horizontal impact. The explanation for this further reduction in the injury level and PoF follows the same biomechanic argumentation as given for (i) above.

Regarding (iii), for DJI Phantom III, DJI F450 and Tarot LJI500, head injury levels are significant factors lower under a 0–45° pitch angle (cases a and b in Table 6) than under a 90° pitch angle (case c in Table 6). To explain the reduced head injury levels, the head acceleration curves for DJI Phantom III, DJI F450, and Tarot LJI500 at a pitch angle of 0° are examined in Figure 19a. All three UAS types induce head acceleration curves with two observable peaks, but these do not appear in the Hypothetical UAS. This is because DJI Phantom III, Tarot and DJI F450 all have a camera gimbal under the fuselage as the first point of contact, while the Hypothetical UAS does not. The camera gimbal system acts as a spring and damper system that dissipates a large amount of impact energy. This gives rise to the first acceleration peak, which represents this energy dissipation from the camera gimbal. Once the camera gimbal is fully compressed, then the motor arms attached to the main UAS fuselage are compressed—giving rise to the second acceleration peak. Notice that the second peak is larger because the main fuselage including the motor arms contains more mass. These two peaks allow the amount of impact energy transfer to be spread out over time, reducing the maximum peak acceleration.

Regarding (iv), for both TrueXS Racing and Parrot Bebop, head injury is significantly higher under a 0–45° pitch angle (cases a and b in Table 7) than under a 90° pitch angle (case c in Table 7). This is because, under a 0° pitch angle, the flat bottom of the fuselage is the first point of contact, resulting in full impact energy transfer in a shorter period than that under a 90° pitch angle, which results in a higher head injury level.

6. Conclusions

This study demonstrated that dynamical modelling and simulation using a multibody system (MBS) framework can effectively assess how the structural stiffness and air-frame design of small UASs influence injury severity and the probability of fatality (PoF) in human head impacts. Five real-world camera–drones—DJI Phantom III, DJI F450, Tarot LJI500, Parrot Bebop, and TrueXS Racing—and with a Hypothetical rigid-body UAS were modelled and evaluated under both controlled horizontal and uncontrolled vertical impact scenarios.

For the horizontal impact scenario at a 151 J kinetic energy, the Hypothetical UAS has a PoF value that is 89% of the PoF value predicted by the RCC parametric model used in standing regulation. For DJI Phantom III, the PoF value further reduces by 2/3 times the RCC's PoF value. For the four UAS types (DJI Phantom III, Tarot LJI500, DJI F450, and True XS Racing), their HIC15 values differ by a factor of 1.5 (=1380/950), and their PoF values differ by a factor of 2.3 (=0.65/0.28). For the horizontal impact scenario, Parrot Bebop can only produce a kinetic energy of 51 J; for this scenario, the PoF assessed for Parrot Bebop is an order of magnitude lower than it is for True XS Racing.

For the uncontrolled vertical impact of a 1.2 kg UAS at 18 m/s on a model of a human head, differences in UAS design yield a difference of up to a factor of 3 in PoF values. Moreover, the highest PoF value is a factor of 2 lower than that under the RCC parametric PoF models used in standing regulation. For the two UAS types measuring 0.4 kg, both factors increase by up to an order of magnitude.

The most critical insight is that initial impact elasticity—whether from the fuselage, motor arms, camera gimbal, or protective materials—largely determines the force transfer to the human head. Designs incorporating flexible elements or soft first-contact surfaces significantly reduce head acceleration and injury severity. These findings reinforce the importance of airframe compliance in UAS safety design.

Compared to Finite Element Method (FEM) simulations, which offer high spatial fidelity at a high computational cost, the MBS approach allows for rapid and accurate prediction of global injury metrics like HIC_{15} and PoF, with each simulation being completed in 10–20 s. This makes MBS modelling a highly practical tool for iterative UAS design evaluation, especially for risk assessment in populated areas.

Although this study is based solely on simulation, the multibody human models used in MADYMO incorporate biomechanical properties validated through experimental cadaver and crash test data. Nevertheless, we recognize the importance of physical validation specific to UAS impacts. A logical next step would be to conduct controlled impact tests using representative UAS configurations with varied materials and structural designs to confirm impact responses. These tests—performed at different velocities and orientations—could provide empirical measurements of head acceleration, HIC_{15}, and PoF, enabling direct comparison with simulation results and helping refine injury prediction models for regulatory use. Such work would be essential to further quantify the relationship between UAS design characteristics and real-world third-party risk.

Future research should extend the MBS framework to include thoracic and abdominal impacts, UASs above 1.2 kg, and fixed-wing configurations. Laceration and penetration injuries—particularly from rotor blades— should be explored by integrating this with human body FEMs that have been developed for application in the automotive domain, e.g., [47]. Additionally, injury response variations across age groups should be considered. While this study used a 50th percentile adult male model, future work should simulate children and elderly individuals, who are likely more susceptible to impact injury. The MADYMO platform supports such anthropometric scaling, and incorporating diverse human body models will further improve the relevance of safety assessments.

Author Contributions: Conceptualisation, B.R., H.A.P.B., D.I.G., M.S. and C.D.W.; methodology, B.R., H.A.P.B. and D.I.G.; software, B.R. and R.H.; validation, B.R. and H.A.P.B.; formal analysis, B.R. and H.A.P.B.; investigation, B.R. and H.A.P.B.; resources, M.S.; data curation, B.R., H.A.P.B., D.I.G., M.S., A.S. and C.D.W.; writing—original draft preparation, B.R. and H.A.P.B.; writing—review and editing, all authors; visualisation, B.R.; supervision, H.A.P.B. and A.S.; project administration, A.S.; funding acquisition, A.S. and M.S. All authors have read and agreed to the published version of the manuscript.

Appendix A

In this appendix, a systematic comparison is made between HIC_{15} levels measured by [22] on the PMHS versus MBS model-based assessments of HIC_{15} levels. The UAS considered in these comparisons is DJI Phantom III. There are three important characteristics of the tests selected from [22,48]:

- The HIC_{15} results from [22] are obtained for male cadavers;
- The test results used from [22] focus on controlled side impacts on the head;
- The results from [22] measure the eccentricity per test.

For DJI Phantom III, the cases from [22] have been simulated using the MBS model under corresponding conditions within MADYMO. More specifically, the following characteristics have been taken into account as follows within MADYMO:

- The scenarios simulated within MADYMO use the impact geometry and impact speed that applied for each test case from [22].
- For the scenarios within MADYMO, the eccentricity used in the MBS simulation is at the same value as that measured for the corresponding test case in [22].

Table A1 compares the weight and standing height of the MADYMO male model used in the simulations, versus those of the three PMHSs used in [22]. Subsequently, Table A2 compares the HIC_{15} results obtained for the cases used from Ohio State University.

The results in Table A1 show that the MADYMO height and weight falls within the range of values of the three PMHS. Comparison against the mean PMHS values shows that the main difference is a 5.1% higher body weight for the MBS model.

Table A1. Comparison of sizes and weights of the MADYMO 50th percentile human male model and the three PMHSs used in [22].

Male Body	PMHS #1	PMHS #2	PMHS #3	PMHS Mean	MBS Male Model [13,25]	Difference
Height	178 cm	168 cm	180 cm	175.3 cm	174 cm	−0.8%
Weight	77.1 kg	73.9 kg	64.9 kg	72.0 kg	75.7 kg	+5.1%

Table A2. Comparison of human HIC_{15} due to the DJI Phantom III impact on the MBS model against the impact test results used in [22].

Impact Case No.	OSU Test	PMHS #	Impact Direction ψ [°]	Impact Elevation θ [°]	UAS Pitch α [°]	Impact Speed, V [m/s]	Eccentricity [mm]	HIC_{15} Test	HIC_{15} MBS	Differ. %	Point of Contact
1	#2	1	90	0	0	17	28.2	866	689	−22.8	Motor Arm
2	#3	1	90	0	0	18.5	17.7	1076	886	−19.4	Motor Arm
3	#4	1	90	0	0	21.5	6.0	2892	2656	−8.5	Fuselage
4	#10	2	90	0	0	18.5	43.4	500	527	+5.3	Motor Arm
5	#11a	2	90	58	58	21.5	42.1	929	828	−11.5	Motor Arm
6	#16a	3	90	58	58	18.5	43.4	412	381	−7.8	Motor Arm
7	#17	3	90	58	58	21.5	20.7	2527	2251	−11.5	Fuselage

Cases no. 1–4 in Table A2 are similar to the controlled horizontal flight impact scenario investigated in Section 4 of the current paper. The MBS estimated HIC_{15} values are lower

for three cases (-22.8%, -19.4% and -8.5%) and higher for one case ($+5.3\%$). On average, the MBS underestimates the HIC_{15} level for these four cases by -11.5%. A similar level of HIC_{15} underestimation by the MBS is found for cases 5–7 in Table A2, in which the impact elevation is $58°$ instead of $0°$.

Because the off-set value is well measured during the PMHS impact tests in [22], the likely explanation for the systematic difference between the HIC_{15} levels for cases 1–7 obtained in [22] versus our simulation results is that our MBS simulation systematically underestimates the HIC_{15} level by 11%. A possible explanation is the slightly higher body weight of the MBS male model compared to the mean weight of the three PMHSs. In view of this, it is best to compensate for the MBS-based estimation of HIC_{15} levels that lead to an 11% systematic underestimation. In the paper, this 11% compensation of MBS-estimated HIC_{15} levels is performed in Sections 4.2 and 5.1 prior to the conversion of HIC_{15} values into PoF values.

References

1. End, A.; Barzantny, C.; Stolz, M.; Grupe, P.; Schmidt, R.; Papenfuß, A.; Eißfeldt, H. Public Acceptance of Civilian Drones and Air Taxis in Germany: A Comprehensive Overview. *CEAS Aeronaut. J.* **2025**, *16*, 665–676. [CrossRef]

2. Glick, T.B.; Figliozzi, M.A.; Unnikrishnan, A. Case Study of Drone Delivery Reliability for Time-Sensitive Medical Supplies with Stochastic Demand and Meteorological Conditions. *Transp. Res. Rec. J. Transp. Res. Board* **2022**, *2676*, 242–255. [CrossRef]

3. El-Adle, A.M.; Ghoniem, A.; Haouari, M. Parcel Delivery by Vehicle and Drone. *J. Oper. Res. Soc.* **2021**, *72*, 398–416. [CrossRef]

4. Benarbia, T.; Kyamakya, K.A. Literature Review of Drone-Based Package Delivery Logistics Systems and Their Implementation Feasibility. *Sustainability* **2021**, *14*, 360. [CrossRef]

5. Mohd Daud, S.M.S.; Mohd Yusof, M.Y.P.; Heo, C.C.; Khoo, L.S.; Chainchel Singh, M.K.; Mahmood, M.S.; Nawawi, H. Applications of Drone in Disaster Management: A Scoping Review. *Sci. Justice* **2022**, *62*, 30–42. [CrossRef] [PubMed]

6. Mogili, U.R.; Deepak, B.B.V.L. Review on Application of Drone Systems in Precision Agriculture. *Procedia Comput. Sci.* **2018**, *133*, 502–509. [CrossRef]

7. Aljalaud, F.; Kurdi, H.; Youcef-Toumi, K. Bio-Inspired Multi-UAV Path Planning Heuristics: A Review. *Mathematics* **2023**, *11*, 2356. [CrossRef]

8. Meng, W.; Zhang, X.; Zhou, L.; Guo, H.; Hu, X. Advances in UAV Path Planning: A Comprehensive Review of Methods, Challenges, and Future Directions. *Drones* **2025**, *9*, 376. [CrossRef]

9. Tutsoy, O.; Asadi, D.; Ahmadi, K.; Nabavi-Chashmi, S.Y.; Iqbal, J. Minimum Distance and Minimum Time Optimal Path Planning with Bioinspired Machine Learning Algorithms for Faulty Unmanned Air Vehicles. *IEEE Trans. Intell. Transp. Syst.* **2024**, *25*, 9069–9077. [CrossRef]

10. JARUS. *SORA v2.0 to v2.5—Summary of Changes for External Consultation. EASA Workshop Presentation Slides*; JARUS: Online, 2023. Available online: https://www.easa.europa.eu/sites/default/files/dfu/sora_workshop_feb_2023_-_4_summary_of_changes_sora.pdf (accessed on 23 July 2025).

11. FAA. *Operation and Certification of Small Unmanned Aircraft Systems*; FAA: Washington, DC, USA, 2016. Available online: https://www.govinfo.gov/content/pkg/FR-2016-06-28/pdf/2016-15079.pdf (accessed on 23 July 2025).

12. JARUS. *Theoretical Basis for Ground Risk Classification and Mitigation, Annex F to Guidelines on SORA*; JARUS: Online, 2024. Available online: http://jarus-rpas.org/wp-content/uploads/2024/06/SORA-v2.5-Annex-F-Release.JAR_doc_29pdf.pdf (accessed on 10 June 2025).

13. RCC (Range Commanders Council). *Range Safety Criteria for Unmanned Air Vehicles, Rationale and Methodology Supplement*. Supplement to Document 323-99. 2001. Available online: https://www.trmc.osd.mil/wiki/download/attachments/113019905/323-99Sup.pdf?version=1&modificationDate=1623181167646&api=v2 (accessed on 15 June 2025).

14. Magister, T. The Small Unmanned Aircraft Blunt Criterion Based Injury Potential Estimation. *Saf. Sci.* **2010**, *48*, 1313–1320. [CrossRef]

15. Toyota Motor Corporation. *Documentation THUMS, AM50 Occupant Model Academic Version 5.0_20150527*. 2015. Available online: https://www.toyota.co.jp/thums/about/ (accessed on 15 June 2025).

16. Happee, R.; Ridella, S. Mathematical Human Body Models Representing a Mid Size Male and a Small Female for Frontal, Lateral and Rearward Impact Loading. In Proceedings of the IRCOBI Conference Proceedings, Montpellier, France, 20–22 September 2000; pp. 1–18.

17. Arterburn, D.; Olivares, G.; Bolte, J.; Prabhu, R.; Duma, S. *Task A14: UAS Ground Collision Severity Evaluation, 2017–2019*; NTIS: Springfield, VA, USA, 2019. Available online: https://assureuas.com/wp-content/uploads/2021/06/A14-Final-Report.pdf (accessed on 23 February 2025).

18. Svatý, Z.; Vrtal, P.; Mičunek, T.; Kohout, T.; Nouzovský, L.; Frydrýn, M.; Blodek, T.; Kocián, K. Impact Analysis Assessment of UAS Collision with a Human Body. *PLoS ONE* **2025**, *20*, e0320073. [CrossRef]

19. Rattanagraikanakorn, B.; Schuurman, M.; Gransden, D.I.; Happee, R.; De Wagter, C.; Sharpanskykh, A.; Blom, H.A.P. Modelling Head Injury Due to Unmanned Aircraft Systems Collision: Crash Dummy vs Human Body. *Int. J. Crashworthiness* **2022**, *27*, 400–413. [CrossRef]

20. Weng, Y.; Bian, K.; Gunasekaran, K.; Gholipour, J.; Vidal, C.; Mao, H. Modeling Small Remotely Piloted Aircraft System to Head Impact for Investigating Craniocerebral Response. *J. Biomech.* **2021**, *128*, 110748. [CrossRef] [PubMed]

21. Toyota Motor Corporation. *Documentation: Total Human Model for Safety AM50 Pedestrian/Occupant Model Academic Version 4.02.* 2018. Available online: https://www.toyota.co.jp/thums/about/ (accessed on 15 June 2025).

22. Stark, D.B.; Willis, A.K.; Eshelman, Z.; Kang, Y.S.; Ramachandra, R.; Bolte, J.H.; McCrink, M. Human Response and Injury Resulting from Head Impacts with Unmanned Aircraft Systems. *Stapp Car Crash J.* **2019**, *63*, 29–64. [CrossRef] [PubMed]

23. Ohio State University. *Annex C: Task A14 UAS Ground Collision Severity Evaluation, Ohio State University Final Report*; NTIS: Springfield, VA, USA, 2019. Available online: https://assureuas.com/wp-content/uploads/2021/06/A14-Annex-C.pdf (accessed on 5 April 2025).

24. Jiang, C.; Blom, H.; Rattanagraikanakorn, B. Enhancing Safety Feedback to the Design of Small, Unmanned Aircraft by Joint Assessment of Impact Area and Human Fatality. *Risk Anal.* **2025**, *45*, 1115–1131. [CrossRef] [PubMed]

25. Wang, J.; Li, Z.; Lan, H.; Cao, L.; Guo, D.; Hao, Z.; Bai, C.; Yang, Z. Study of the Head and Neck Injury Risk under Impact Conditions of the Light UAV with a Medium Weight. *Arch. Civ. Mech. Eng.* **2023**, *23*, 226. [CrossRef]

26. Li, R.; Li, Z.; Lan, H.; Bai, C.; Guo, Y.; Wang, Y.; Wang, J.; Liu, X.; Yang, Z. Study on the Head and Neck Injury Risk Impacted by UAV: Effect of Impact Velocity, Angle, Location, and Mass. *Int. J. Crashworthiness* **2024**, *29*, 482–494. [CrossRef]

27. Rattanagraikanakorn, B.; Gransden, D.I.; Schuurman, M.; De Wagter, C.; Happee, R.; Sharpanskykh, A.; Blom, H.A.P. Multi-Body System Modelling of Unmanned Aircraft System Collisions with the Human Head. *Int. J. Crashworthiness* **2020**, *25*, 689–707. [CrossRef]

28. Rattanagraikanakorn, B. Modelling Collisionconsequences of Unmanned Aircraft Systems on Human. Ph.D. Thesis, Delft University of Technology, Delft, The Netherlands, 2021.

29. Brake, M.R. An Analytical Elastic-Perfectly Plastic Contact Model. *Int. J. Solids Struct.* **2012**, *49*, 3129–3141. [CrossRef]

30. TASS International. *MADYMO Theory Manual, Version 7.7*; TASS International: Helmond, The Netherlands, 2017.

31. TASS International. *MADYMO Human Body Models Manual, Release 7.7*; TASS International: Helmond, The Netherlands, 2017.

32. Klinich, K.; Saul, R.; Auguste, G.; Backaitis, S.; Kleinberger, M. Techniques for Developing Child Dummy Protection Reference Values. *Measurement*. 1996. Available online: https://rosap.ntl.bts.gov/view/dot/14741/dot_14741_DS1.pdf (accessed on 15 June 2025).

33. Seacrist, T.; Balasubramanian, S.; García-España, J.F.; Maltese, M.R.; Arbogast, K.B.; Lopez-Valdes, F.J.; Kent, R.W.; Tanji, H.; Higuchi, K. Kinematic Comparison of Pediatric Human Volunteers and the Hybrid III 6-Year-Old Anthropomorphic Test Device. *Ann. Adv. Automot. Med.* **2010**, *54*, 97–108. [CrossRef]

34. Seacrist, T.; Samuels, M.; García-España, J.F.; Arbogast, K.B.; Mathews, E.A.; Balasubramanian, S.; Maltese, M.R.; Longhitano, D.; St. Lawrence, S. Kinematic Comparison of the Hybrid III and Q-Series Pediatric ATDs to Pediatric Volunteers in Low-Speed Frontal Crashes. *Ann. Adv. Automot. Med.* **2012**, *56*, 285–298. [CrossRef] [PubMed]

35. Li, H.; Lv, W.; Hynčík, L.; Zhou, B.; Zhao, H.; Cui, S.; He, L.; Ruan, S. Injury Study of the 6-Year-Old Pediatric Thorax and Abdomen in Frontal Sled Tests Using Different Computational Models. *Front. Future Transp.* **2022**, *3*, 890776. [CrossRef]

36. Parr, M.J.C.; Miller, M.E.; Bridges, N.R.; Buhrman, J.R.; Perry, C.E.; Wright, N.L. Evaluation of the Nij Neck Injury Criteria with Human Response Data for Use in Future Research on Helmet Mounted Display Mass Properties. In Proceedings of the 56th Human Factors and Ergonomics Society Annual Meeting, Boston, MA, USA, 22–26 October 2012; pp. 2070–2074. [CrossRef]

37. Schmitt, K.-U.; Niederer, P.F.; Cronin, D.S.; Morrison, B., III; Muser, M.H.; Walz, F. *Trauma Biomechanics*; Springer: Cham, Switzerland, 2019.

38. Tyrell, D.C.; Severson, K.J.; Marquis, B.P. Analysis of Occupant Protection Strategies in Train Collisions. In *Proceedings of the ASME International Mechanical Engineering Congress and Exposition*; San Francisco, CA, USA, 12–17 November 1995. Available online: https://rosap.ntl.bts.gov/view/dot/8520 (accessed on 11 November 2024).

39. Prasad, P.; Mertz, H.J. *The Position of the United States Delegation to the ISO Working Group 6 on the Use of HIC in the Automotive Environment*; SAE Technical Paper; SAE: Warrendale, PA, USA, 1985.

40. Rattanagraikanakorn, B.; Blom, H.A.P.; Sharpanskykh, A.; de Wagter, C.; Jiang, C.; Schuurman, M.J.; Gransden, D.I.; Happee, R. Modeling and Simulating Human Fatality Due to Quadrotor UAS Impact. In Proceedings of the AIAA AVIATION 2020 FORUM, Online, 15–19 June 2020. [CrossRef]

41. Parrot Drones SAS. All-In-One Drone Solution for 3D Modeling (Parrot Bebop-Pro 3D Modeling Product Sheet). Online. 2018. Available online: https://www.parrot.com/assets/s3fs-public/2021-09/bat_parrot_productsheet_power_bb-3d-modelling_a4_2018-01-08_en.pdf (accessed on 10 October 2019).

42. FPV Drone Reviews. Top 5 Fastest Racing Drones of 2018—Buying Guide. Online. 2018. Available online: https://fpvdronereviews.com/guides/fastest-racing-drones/ (accessed on 10 October 2019).

43. Belcastro, C.M.; Newman, R.L.; Evans, J.; Klyde, D.H.; Barr, L.C.; Ancel, E. Hazards Identification and Analysis for Unmanned Aircraft System Operations. In Proceedings of the 17th AIAA Aviation Technology, Integration, and Operations Conference, Denver, CO, USA, 5–9 June 2017. [CrossRef]

44. Foster, J.V.; Hartman, D.C. High-Fidelity Multirotor Unmanned Aircraft System Simulation Development for Trajectory Prediction under off-Nominal Flight Dynamics. In Proceedings of the 17th AIAA Aviation Technology, Integration, and Operations Conference, Denver, CO, USA, 5–9 June 2017. [CrossRef]

45. Arterburn, D.; Ewing, M.; Prabhu, R.; Zhu, F.; Francis, D. *FAA UAS Center of Excellence Task A4: UAS Ground Collision Severity Evaluation*; ASSURE: Huntsville, AL, USA, 2017. Available online: https://assureuas.com/wp-content/uploads/2021/06/A4-Final-Report.pdf (accessed on 17 May 2025).

46. Bernard, E.; Johnston, A. Explosions and Blast Injuries—A Primer for Clinicians. *N. Engl. J. Med.* **2013**, *368*, 1045. [CrossRef]

47. Fahlstedt, M.; Halldin, P.; Kleiven, S. Comparison of Multibody and Finite Element Human Body Models in Pedestrian Accidents with the Focus on Head Kinematics. *Traffic Inj. Prev.* **2016**, *17*, 320–327. [CrossRef] [PubMed]

48. ASSURE. *Annex B: NIAR Final Report—Task A14: UAS Ground Collision Severity Evaluation 2017–2018*; NTIS: Springfield, VA, USA, 2019. Available online: https://assureuas.com/wp-content/uploads/2021/06/A14-Annex-B.pdf (accessed on 23 July 2025).